

Detection and Measurement of Parsec-Scale Circular Polarization in Four AGN

D. C. Homan¹ and J. F. C. Wardle²

Department of Physics, Brandeis University, Waltham, Massachusetts 02454, USA

Appeared in the Astronomical Journal, Nov 1999, vol 118, pg 1942

ABSTRACT

We present five epochs of 15 GHz VLBA observations of 13 AGN. These observations were specially calibrated to detect parsec-scale circular polarization and our calibration techniques are discussed and analyzed in detail. We obtained reliable detections of parsec-scale circular polarization in the radio jets of four AGN: 3C 84, PKS 0528+134, 3C 273, and 3C 279. For each of these objects our detections are at the level of $\sim 0.3 - 1\%$ local fractional circular polarization. Each individual detection has a significance in the range of 3 to 10 σ . Our observations are consistent across multiple epochs (and different calibration techniques) in the sign and magnitude of the circular polarization observed. 3C 273 and 3C 279 both undergo core outbursts during our observations and changes in the circular polarization of both sources are correlated with these outbursts. In general, we observe the circular polarization to be nearly coincident with the strong VLBI cores of these objects; however, in 3C 84 the circular polarization is located a full milli-arcsecond south of the source peak, and in the 1996.73 epoch of 3C 273 the circular polarization is predominately associated with the newly emerging jet component. Our observations support the theoretical conclusion that emission of circular polarization is a sensitive function of opacity, being strongest when the optical depth is near unity. Circular polarization may be produced as an intrinsic component of synchrotron radiation or by the Faraday conversion of linear to circular polarization. Our single frequency observations do not easily distinguish between these possible mechanisms, but independent of mechanism, the remarkable consistency across epoch of the sign of the observed circular polarization suggests the existence of a long term, stable, uni-directional magnetic field. Single dish observations of 3C 273 and 3C 279 at 8 GHz by Hodge and Aller suggest that this stability may persist for decades in our frame of observation.

Subject headings: galaxies: jets — galaxies:magnetic fields — polarization — quasars: individual (3C 84, PKS 0528+134, 3C 273, 3C 279)

¹dch@quasar.astro.brandeis.edu

²jfcw@quasar.astro.brandeis.edu

1. Introduction

The detection and measurement of circular polarization in compact, extra-galactic radio sources has long been a difficult observational challenge. The first reliable observations of integrated circular polarization were made by Gilbert and Conway (1970) at 49 cm. Weiler and de Pater (1983) cataloged and reviewed integrated measurements of circular polarization in a large number of extra-galactic radio sources. They found no reliable measurements above 0.5% with the majority of the observations $\lesssim 0.1\%$. Jones (1988) used numerical simulations to model relativistic jets in compact radio sources and found that the *local* fractional circular polarization could be much higher than 0.5%.

Circular polarization may be produced either as an intrinsic component of synchrotron radiation or by Faraday conversion of linear to circular polarization (e.g. Jones & O’Dell 1977). Intrinsic circular polarization is produced directly by the radiating particles and serves as a probe of the magnetic field structure along the line of sight. Faraday conversion, however, is a propagation effect, dominated by the lower energy relativistic particles in the jet, and therefore serves as a probe of the low energy end of the relativistic particle distribution.

We present observations of parsec-scale circular polarization in four compact, extra-galactic radio sources. These observations were part of an ongoing program to monitor the structure and polarization of 12 rapidly variable compact radio sources, using the Very Long Baseline Array (VLBA) at $\lambda 1.3$ cm (22 GHz) and $\lambda 2$ cm (15 GHz). The circular polarization observations presented in this paper were made at 15 GHz. Observations were made at intervals of two months, and the consistency between images made at different epochs is an important check on our results.

We have detected circular polarization in 3C 84, PKS 0528+134, 3C 273, and 3C 279 at 15 GHz. We find each of these sources to have local circular polarization at levels of 0.3% to 1%. These observations are consistent across multiple epochs, and display changes linked with core outbursts in 3C 273 and 3C 279.

To make these observations we have devised three separate calibration and imaging techniques, described in brief in section 3. Detailed discussion and analysis of these techniques and other issues important to the measurement of circular polarization is postponed to the appendix. The details of our experiments and a brief description of our calibration procedures are provided in section 2. Section 4 presents results on all the sources in our sample and images of four of them. We discuss the reliability of our calibration in §5 and the physical interpretation of our observations in §6. Our conclusions are presented in section 7.

2. Observational Details

The observations presented here were part of a project to monitor closely a sample of 13 AGN at 15 and 22 GHz with the VLBA.³ The sources were observed at two month intervals from January 1996 to December 1996, for a total of 6 epochs. We present the 15 GHz circular polarization observations from the first 5 epochs. (Re-calibration for circular polarization of the 22 GHz companion observations is currently in progress.) The overall data quality of the sixth epoch is much poorer than the previous five making reliable detection of circular polarization difficult. Table 1 lists the five epochs for which we present data in this paper. Table 2 is a list of the 13 sources monitored with these observations.

The observations were scheduled to maximize coverage in the u-v plane. To accomplish this goal, scan lengths were kept short (6.5 minutes per scan for the first two epochs and 5.5 minutes per scan for the remaining epochs) and frequencies were switched following every scan. In addition, scans of neighboring sources were heavily interleaved at the expense of some additional slew time. Each source received approximately 45 minutes per frequency of observation time at each epoch.

The data were recorded at each antenna using 1-bit sampling and were correlated at the VLBA correlator in Socorro, NM. The correlator output contained 2 second integrations for all four cross-correlations (RR, RL, LR, LL), each with 4 IFs and 16 channels per IF. The data were distributed on DAT tape to Brandeis University where they were loaded into NRAO’s Astronomical Imaging Processing System (AIPS).

Following a careful inspection of the data and supplied tables, the task UVFLG read in the supplied flagging information and applied the initial edits. The parallactic angles were then removed from the data with the task CLCOR. Prior to fringe fitting, the supplied pulse calibration information was applied with the task PCCOR.⁴ Global fringe fitting was performed with the AIPS task FRING, choosing a stable, central reference antenna such as Los Alamos (LA) or Pie Town (PT). The AIPS procedure CROSSPOL then removed the multi-band delay difference between the right and left hand systems of the array. Initial amplitude calibration was from measured system temperatures and atmospheric opacity (using the tasks ANTAB and APCAL). A bandpass correction was then determined with the task BPASS before averaging across the channels within each IF.

Following a short time-scale point source⁵ phase calibration to increase coherence, the data were averaged in time to 20 seconds and written out to the Caltech VLBI program, DIFMAP. The

³The National Radio Astronomy Observatory is operated by Associated Universities, Inc., under cooperative agreement with the National Science Foundation.

⁴The only exception is epoch 1996.05, where a manual phase calibration was used to align the phases across IF.

⁵After epoch-A, the source model from a previous epoch was used in place of a point source model for the initial phase coherence calibration.

data were then edited in a station based manner. At this point, a copy of the data was written out to disk; this data will be referred to as the edited, un-self-calibrated data. Within DIFMAP, standard imaging and self-calibration techniques were applied to obtain the best possible total intensity model. This model was then written out to AIPS and used to self-calibrate the edited, un-self-calibrated data (using first a 20 second solution interval for phase calibration followed by a 10 minute solution interval for amplitude calibration).

Following additional phase self-calibration passes in AIPS, the effects of feed leakage (D-terms) were removed from the parallel and cross hand data. This is crucial since the D-terms induce non-closing errors in the RR and LL data that are not removed by self-calibration and could mimic a circularly polarized signal. On a single baseline scan these errors are of order D^2 for an unpolarized source and $m_L D$ for a polarized source, where m_L is the fractional linear polarization. (See §A.1 for a detailed analysis.)

The antenna D-terms were determined from observations of the strong, compact source PKS 0528+134, using the program LPCAL⁶ in AIPS (Leppänen, Zensus, & Diamond 1995). The amplitudes of the D-terms ranged from approximately 1% to 5% with values close to 2% being most typical. As described in §A.1, our D-term calibration is accurate enough to limit D-term related errors in our circular polarization images to less than 0.2% of the corresponding linear polarization.

After D-term removal, a further amplitude self-calibration was applied using the initial total intensity model from DIFMAP. This is important to remove any amplitude gain errors made by the amplitude self-calibration prior to removal of the D-terms. A final round of phase self-calibration was performed before imaging in all four Stokes parameters. These images were made in the usual way and are presented in Section 4.

3. Circular Polarization Calibration

The calibration steps described above are similar to those used for any VLBA observation designed to measure linear polarization (Cotton 1993; Roberts, Wardle, & Brown 1994). For circular polarization, we must also carefully consider the relative calibration of the right (R) and left (L) complex antenna gains. Appendix A.2 explores this issue in depth; here we briefly summarize our three separate techniques for calibrating the R and L complex antenna gains.

⁶The D-terms found by LPCAL are in the linear feed model. Versions of AIPS prior to the April 15, 1997 release require D-terms to be in the ellipticity-orientation model if they are to be applied to all four complex correlations. For this reason, it was necessary to translate the D-terms to the ellipticity-orientation model prior to their application.

3.1. Gain Transfer

In this technique, we initially make no assumption about the presence or absence of circular polarization in our sources. All self-calibration rounds are performed with the rigorous assumption $(RR + LL)/2 = \tilde{I}_{model}$. This assumption will calibrate only the average of R and L at a given antenna, leaving the relative R/L antenna gain ratio completely uncorrected.

At the end of the calibration only the R/L gain ratios remain to be calibrated before we can make circular polarization images. If we know that some of our sources have no circular polarization, we can calibrate this ratio on these sources by doing a final self-calibration with the assumption: $RR = \tilde{I}_{model}$ and $LL = \tilde{I}_{model}$.

We found these corrections (one per scan in amplitude and phase) on the subset of sources which appeared to have no circular polarization (see §A.2.2 for discussion of how these sources were determined.). The corrections were then averaged and smoothed on a 4 hour time scale before application to all sources in the sample. The errors in this technique are dominated by the short-term (scan-to-scan) R/L gain fluctuations. Analyzed in §A.2.2, these fluctuations can limit the sensitivity of this technique to $\lesssim 0.15\%$ of the local total intensity. The errors listed in the tables of results were derived using equation A20 and we believe they provide a conservative estimate of the 1σ uncertainty.

Circular polarization images produced from data calibrated with this technique are referred to in the text as *gain transfer* images. Making images in this way depends critically on the stability of the antenna gains. It is a tribute to the outstanding performance of the VLBA that such images are now possible.

3.2. Zero-V Self-calibration

Another technique is to perform all self-calibration rounds with the assumption that there is no real circular polarization (Stokes V) in the data. In this calibration scheme, separate complex gain corrections are found for the R and L hands at each antenna by assuming $RR = \tilde{I}_{model}$ and $LL = \tilde{I}_{model}$. This assumption will try to reduce any circular polarization (real or spurious) as much as possible by adjusting the complex antenna gains. We will refer to this calibration technique as *zero-V self-calibration*.

Real circular polarization is additive in the RR and LL correlations while the complex gains are multiplicative. Therefore, if a source has significant extended structure, *zero-V self-cal* will not be able to completely remove real circular polarization from the source. In general, if the strong core of a source has real circular polarization, this procedure will remove the circular polarization from the strong core and transfer it (with reverse sign but the same local fractional level) to the weaker extended structure. If the circular polarization is originally on the weaker extended structure (rather than the core), *zero-V self-cal* cannot modify it much without inducing

significant circular polarization on the core.

3.3. Phase-Only Mapping

The previous two calibration techniques, *gain transfer* and *zero- V self-cal*, are subject to errors in the antenna amplitude gains. The idea behind *phase-only* mapping is to demonstrate that any circular polarization detected by these techniques is also present (in a consistent manner) in the phases of the data alone. If a source has real circular polarization, then the RR and LL closure phases will be slightly different, and this difference is preserved throughout the calibration process. For simple sources, we can even use the *phase-only* image to predict the amplitudes of circular polarization measured by the other techniques.

To construct a *phase-only* image, we set the amplitudes of the RR and LL correlations to unity and construct the V visibilities from the resulting “phase-only” correlations. Naturally, if the source is a simple point source or has no real circular polarization, this technique will not detect any circular polarization. For simple sources with extended structure and real circular polarization, *phase-only* mapping produces circular polarization images that are anti-symmetric (to first order) at the jet position around the location of the core.

To construct *phase-only* images that are not dominated by short-term phase noise fluctuations ($\sim 0.2^\circ$) between the R and L hands at each antenna, we found that the phases must be self-calibrated with the assumption $RR = \tilde{I}_{model}$ and $LL = \tilde{I}_{model}$. However, as should be expected, the *phase-only* images did not at all depend on how the amplitudes were corrected: calibrating the amplitudes by assuming either $(RR + LL)/2 = \tilde{I}_{model}$ or $RR = \tilde{I}_{model}$, $LL = \tilde{I}_{model}$ produces identical results.

4. The Observations

Of the 13 observed sources, we have reliable detections of circular polarization on four: 3C 84 (J0319+41), PKS 0528+134 (J0530+13), 3C 273 (J1229+02), and 3C 279 (J1256-05). The 15 GHz observations of these four sources are presented individually. The 15 GHz observations of the remaining 9 sources are presented as a group.

4.1. 3C 279 (J1256-05)

Images for the 1996.05 epoch of 3C 279 in total intensity, linear polarization, and circular polarization are presented in Figure 1. The circular polarization image was produced with the *gain transfer* calibration technique (§3.1). The images are very similar to those from the later epochs (see Wardle et al. (1998) for images from the 1996.57 epoch), although the core increases

in strength (as does the circular polarization) in the later epochs. The images display a strong, compact core with a jet extending to the southwest at position angle -113 degrees. There is a bright knot in the jet at approximately 3 milli-arcseconds from the core.

The core has modest fractional linear polarization ($m_L = 4.1\%$). The observed integrated circular polarization on the core is 36 mJy, corresponding to +0.3% local fractional circular polarization. While this measurement superficially constitutes a 30σ detection when compared to the RMS noise on the map, analysis of the *gain transfer* technique in §A.2.2 shows that such measurements are limited by short time-scale gain fluctuations. The associated errors in the *gain transfer* circular polarization maps may be as large as 0.15% of the corresponding total intensity. Values obtained by the other calibration techniques (described below), however, increase our confidence that our circular polarization measurement for epoch 1996.05 is accurate to a few milliJanskys.

Detailed, u-v plane model-fitting of the core region in total intensity and linear polarization (at both 15 and 22 GHz), reveals that the core consists of two closely spaced (~ 0.1 mas) components. In Wardle et al. (1998) we argue that circular polarization is associated with the western core component (CW) in the 1996.57 epoch. Assuming this association holds for the other epochs, CW is +1.2% circularly polarized in epoch 1996.05. The core fluxes and polarizations for all five epochs are given in Table 3.

3C 279 provides our most robust circular polarization observations. As a result of its relatively simple, (unequal) point double morphology on milli-arcsecond scales, all three of our calibration techniques give readily interpretable and consistent results. Figure 2 displays the circular polarization images as produced by our three calibration techniques in epoch 1996.05.

Figure 2a displays the image produced by our *gain transfer* calibration procedure. The image is the same as in Figure 1 except that it has a different boundary for easy comparison to Figures 2b and 2c, produced by our other calibration procedures. In epoch 1996.05, the integrated core circular polarization measured by the *transfer of gains* calibration is +36 (± 18) mJy.

Figure 2b displays the image produced by the *zero-V self-cal*, calibration procedure. The circular polarization signal detected by this technique is located on the bright knot in the jet at the -0.3% level. As explained in §A.2.1, self-calibration assuming zero circular polarization will transfer circular polarization from the strong core of an unequal point double (like 3C 279) to the weaker jet component at the same local fractional level but with reversed sign. Assuming the circular polarization truly lies on the core (as revealed by the *gain transfer* calibration technique), we can extrapolate the core circular polarization from the observed jet circular polarization by modeling the source as a simple point double and using the relation, $V_1 \simeq -V_2(I_1/I_2)$ (see §A.2.1). Applying this simple relation to epoch 1996.05, gives an integrated core circular polarization of +32 (+9, -3) mJy.

Figure 2c displays the image produced by our *phase-only* method. The circular polarization detected by this technique is anti-symmetric about the core with the jet knot location. The

integrated intensities of $-228 \mu\text{Jy}$ for the jet and $+198 \mu\text{Jy}$ for the anti-jet from the phase-only data can be used to predict the core circular polarization, using equation A22 (§A.2.3) and assuming a simple point double model for 3C 279. Applying this relation to epoch 1996.05, gives an integrated core circular polarization of $+27 (+7, -2) \text{ mJy}$.

It is important to note that the errors associated with the *zero-V self-cal* and *phase-only* measurements of circular polarization reflect not only random noise but also the possible systematic loss of signal, described in §A.2.1, associated with assuming no circular polarization at one or more steps in the self-calibration process.

The *gain transfer*, *zero-V self-cal*, and *phase-only* maps from the later epochs are very similar to those displayed in Figure 2 for epoch 1996.05. Table 4 displays the raw measurements of circular polarization from the *zero-V self-cal* and *phase-only* calibration techniques. Table 5 summarizes the results from applying a simple point double model to these raw measurements and extrapolating the circular polarization of the core. The extrapolations are compared to the more direct *gain transfer* results. Figure 3 compares the results from the three calibration techniques.

4.2. 3C 84 (J0319+41)

Figure 4 displays images for the 1996.74 epoch of 3C 84 in both total intensity and circular polarization structure. 3C 84 has a strong core which is elongated in the north-south direction. The jet extends to the south forming a diffuse lobe-like region about 10 mas south of the core. To the north we clearly detect the counter feature reported by Vermeulen, Readhead, and Backer (1994) and Walker, Romney, and Benson (1994). The total intensity structure of 3C 84 does not appear to change significantly over the course of our observations. The linear polarization structure (not shown) of 3C 84 is very weak. Only the “lobe” shows significant linear polarization in a couple isolated spots at the 1% local level.

Figure 4b is produced by *zero-V self-calibration* and clearly shows the circular polarization structure to lie in the south-eastern part of the elongated core at approximately the +1% ($\pm 0.1\%$) level. A smaller, negative piece of circular polarization is located just north and west of the positive circular polarization. In §A.2.1, we show that *zero-V self-cal* does very little to modify the circular polarization in a source if it is well separated from the main peak in total intensity. Here the *V* peak is only one beam-width south of the *I* peak, and we believe the negative component is an artifact resulting from the *zero-V self-calibration* assumption. We were indeed able to produce just such a negative signal by *zero-V self-cal* in simulated data sets of 3C 84. The images produced by *zero-V self-cal* in the other epochs are essentially the same as figure 4b, each revealing about +1% ($\pm 0.1\%$) local circular polarization in the same location.

The *gain transfer* and *phase-only* images are presented in Figure 5. They are both very consistent with the *zero-V self-cal* result. The *gain transfer* image (Figure 5a) shows the positive circular polarization to be stronger (28 versus 18 mJy/beam) than the *zero-V self-cal* image. The

smaller, negative circular polarization is also shown by the *gain transfer* image, although it is much weaker and located more to the west rather than to the north-west as indicated by the *zero-V self-cal* image.

The other epochs show generally consistent *gain transfer* results, although the quality of the *gain transfer* results vary from epoch to epoch. The circular polarization signals measured by *gain transfer* are always in the same location (south and east of the map peak) and are usually within a couple of mJy of the *zero-V self-cal* result. The worst *gain transfer* result is the 1996.57 epoch which has large pits and valleys in the circular polarization image, masking the circular polarization signal clearly detected by the other two techniques.

Figure 5b is the *phase-only* circular polarization image of 3C 84 in the 1995.74 epoch. The result is difficult to interpret directly due to the extreme complexity of the source. However it is clear that this image is consistent with the results produced by the other two techniques. The *phase-only* results from the other epochs are equally consistent.

4.3. PKS 0528+134 (J0530+13)

The total intensity, linear polarization, and circular polarization images of PKS 0528+134 from our 1996.57 epoch are presented in Figure 6. The total intensity and circular polarization observations from the other epochs are very similar to those presented. The linear polarization, however, changes considerably over the course of our observations. PKS 0528+134 is a barely resolved point source with an extension to the NNE. In tapered images we observe extended flux approximately 3 milli-arcseconds to the NNE, suggesting that the parsec-scale jet extends in that direction. The circular polarization (as revealed by the *gain transfer* calibration technique) lies directly on the core with an integrated intensity of $+45 \text{ mJy} \pm 10 \text{ mJy}$ ($m_c = +0.6\%$). The circular polarization maps for the other epochs are very similar, each revealing strong positive circular polarization: $+40$ to $+50 \text{ mJy}$ in three of the other epochs and $+100 \text{ mJy}$ in one epoch.

Our model-fitting of the total intensity data reveals the core to consist of two closely spaced components, however the linear polarization structure is fit quite poorly by this model. We cannot associate the circular polarization with either of these total intensity model components with any confidence. As a result, we will treat the core as a single component with the associated linear and circular polarization. Table 6 contains the integrated measurements of total intensity, linear polarization, and circular polarization for the core of PKS 0528+134 for each of the five epochs presented in this paper.

Zero-V self-cal and *phase-only imaging* both revealed no detectable circular polarization on PKS 0528+134. As explained in §A.2, neither of these techniques would detect circular polarization on what is essentially a point source. However, we are confident that the circular polarization revealed in the *gain transfer* images is real.

4.4. 3C 273 (J1229+02)

Figure 7 displays the total intensity, linear polarization, and circular polarization images of 3C 273 for the 1996.41 epoch. In these images 3C 273 has a strong core with a bright jet extending at a position angle of $\sim -120^\circ$. The core has weak linear polarization at the 0.3% level, and the jet is more strongly polarized at the $\simeq 10 - 40\%$ level. The observed circular polarization lies directly on the core with an integrated intensity of $-74 \text{ mJy} \pm 15 \text{ mJy}$ ($m_c = -0.6\%$).

The total intensity and linear polarization structure of the jet are very similar in the other epochs. The integrated flux density of the core, however, increases in strength from epoch 1996.05, where it is 2.8 Jy, to epoch 1996.57, where it is 13.4 Jy. By epoch 1996.74, the core is clearly comprised of two components (denoted CE and CW in Table 7). We report the results of u-v plane model-fitting of the core region for each epoch in Table 7.

The circular polarization structure of the core also changes over the course of the epochs in a manner consistent with the total intensity and linear polarization changes. In epoch 1996.05, the integrated circular polarization is $-10 \text{ mJy} \pm 10 \text{ mJy}$ ($m_c \sim -0.4\%$ but consistent with zero) in a very noisy *gain transfer* image. At epoch 1996.23, the total intensity of the core is much higher, but we detect no circular polarization with a limit $< 0.2\%$. In 1996.41 (Figure 7), the circular polarization is -0.6% and the core also shows the first signs of linear polarization. In 1996.57, the circular polarization is -0.5% and the linear polarization has increased further. By 1996.74 the core has split in total intensity and linear polarization; the circular polarization also splits and is predominately associated with the western core (CW) component. Figure 8 displays uniformly weighted total intensity, linear polarization, and circular polarization images from the 1996.74 epoch.

Figure 9 displays the circular polarization images produced by the *gain transfer*, *zero-V self-cal*, and *phase-only* calibration procedures for epoch 1996.41. Figure 9a is the *gain transfer* image presented in Figure 7c, framed differently for ease of comparison to the other images. Figure 9b is the *zero-V self-cal* image. It is clear that the circular polarization from the core has been transferred (by self-calibration) to the jet with reversed sign and much reduced (absolute) level. Figure 9c is the *phase-only* image. As expected, the signal in the phase-only map is anti-symmetric about the core with respect to the jet location.

Due to the complexity of 3C 273, it is difficult to use the *zero-V self-cal* and *phase-only* calibration techniques to derive firm numbers for the true circular polarization of 3C 273. The best numbers are derived from the *gain transfer* calibration procedure, but it is clear that the *zero-V self-cal* and *phase-only* images are consistent with the *gain transfer* results. The 1996.57 and 1996.74 epochs also produce *zero-V self-cal* and *phase-only* images consistent with the results from *gain transfer* calibration.

4.5. Other Sources

Circular polarization observations (using *gain transfer* calibration) from our remaining nine sources are summarized in Table 8. In most cases, these sources show no circular polarization from any of our calibration techniques. The upper limits and errors reported in Table 8 are estimated to be roughly $\sqrt{2}$ times the noise peaks on the circular polarization images. It is interesting to note that, in general, the upper limits estimated from noise peaks are consistent with the estimate of expected error of $\lesssim 0.15\%$ due to short term gain fluctuations (derived in §A.2.2).

In isolated epochs, a few of the sources (J0738+17, J1512-09, J1751+09, J1927+73, and J2005+77) appear to exhibit some core circular polarization. In all of these sources, except J1927+73, the detected core circular polarization is comparable to the peak noise in the image. In the three epochs in which it is detected, the circular polarization signal for core of J1927+73 is significantly larger than the peak noise.

5. Reliability of Calibration and Detection

In appendix A, we analyze in detail the calibration for circular polarization. Here we provide a more general discussion of the reliability of our calibration and claims of detection of circular polarization.

Chief among the sources of spurious circular polarization are antenna feed leakage (D-terms) and improper gain calibration. Our analysis in §A.1 demonstrates that the D-terms, even if completely uncorrected, cannot be the source of the circular polarization we observe. Our correction of the D-terms is accurate enough to limit feed leakage errors in of circular polarization images to 0.2% of the linear polarization (which itself is typically only a few percent of the corresponding total intensity). The antenna D-terms are not a factor in the reliability or quality of our results.

In §A.2, we describe the three gain calibration techniques we have used to detect and measure circular polarization. Two of these techniques, *gain transfer* and *zero-V self-cal*, derive independent measures of the R versus L antenna gains. The third technique, *phase-only* imaging, is independent of the antenna amplitude gains and is used to demonstrate that a circular polarization signal is also present in the phases of the data.

The *zero-V self-cal* technique can reduce or relocate existing circular polarization. This technique assumes that there is no true circular polarization on the source in question, i.e. that $RR = \tilde{I}_{mod}$ and $LL = \tilde{I}_{mod}$. As a result, true circular polarization can be modeled in part or in whole as a gain error and removed from the data. On a point source any true circular polarization will be completely removed by this technique; however, the same is not true for more complicated sources. Because true circular polarization is additive in the RR and LL correlations, it cannot be completely “corrected” by multiplicative antenna gains.

For a typical source with a strong core and a much weaker jet, circular polarization from the core of the source will be *transferred* by the derived antennas gains (which try to minimize the overall circular polarization) to the weaker parts of the source, with reversed sign, and at (roughly) the same local fractional level. With the notable exception of 3C 279, most sources are too complicated to directly disentangle this effect and derive the true circular polarization of the source. (Extended trial and error simulations could, in principle, reconstruct the original circular polarization distribution.) Also, if the true circular polarization is located in the weaker jet (as in 3C 84), then *zero-V self-cal* does much less to modify it.

The *gain transfer* technique provides our most direct measurement of circular polarization. The R/L gain ratios applied to 3C 84, J0530+13, 3C 273, and 3C 279 were derived from the remaining nine sources. As a result, no assumption was made about the presence of circular polarization on these four sources. However, in this procedure, the antenna gains applied to the other nine sources are not really source independent. To what extent can we trust the results of the *gain transfer* on these sources?

The sources in our observation were highly interleaved to maximize u-v coverage. This fact, coupled with our four hour averaging interval for the derived gain table, helps to make the gain table largely independent of individual sources. As described in §A.2.2, we tested this assumption and found very nearly the same results when the sources which have circular polarization are allowed to contribute their gain corrections. We conclude that the results on these other sources, which were allowed to contribute to the gain table, can be trusted within the quoted errors.

One danger in the *gain transfer* technique is that the R/L antenna gains may not be stable on time scales long enough to allow their transfer. Our results demonstrate that the gains are indeed stable enough to produce reliable results. The observed circular polarizations are consistent in terms of sign, location, and amplitude from epoch to epoch. (See Figure 10.) We would not expect this consistency if the R/L antenna gains were not stable on time scales of at least several hours. It is important to note that the consistency is not perfect. This is partly due to source variability, but may also reveal limits to the reliability of this technique. In fact, our main source of error in this technique is short time scale gain fluctuations which go uncorrected. Section A.2.2 provides an estimate of the errors from these fluctuations.

An important point is that the strong negative circular polarization observed on 3C 273 increases our confidence in the *gain transfer* calibration technique. 3C 273 and 3C 279 are neighbors in the sky and interleaved in our observation schedule. Due to the four hour averaging time, they will receive essentially the same set of R/L antenna gains. Any bias in the antenna gains would be expected to have the same effect on both sources; however, they have circular polarizations of *opposite* sign.

The consistency between all of our techniques is best evaluated with 3C 279 where we can use a simple point double model to directly compare the results of all three approaches. As demonstrated by our results in table 5 (graphically displayed in figure 3), these techniques always

agree that a signal was detected and on the sign of that signal. Furthermore, the techniques agree in amplitude to within a factor of two (and often much better than that).

6. Physical Interpretation

Circular polarization may be produced as an intrinsic component of synchrotron radiation or by Faraday conversion of linear to circular polarization (e.g. Jones & O’Dell 1977). Determining which mechanism produces the circular polarization we observe is crucial to using the observations as a physical probe of parsec-scale radio jets. Intrinsic circular polarization demands a significant uni-directional component of magnetic field while Faraday conversion requires a significant population of low energy relativistic particles in the jet (Wardle et al. 1998).

In Wardle et al. (1998) we analyze the 1996.57 epoch of 3C 279 in detail and use limits on the circular polarization present in the 22 GHz companion observations to show that Faraday conversion is the origin of the circular polarization observed in that source. Our results set an upper limit on the low energy cutoff to the relativistic particle distribution of $\gamma_{min} \leq 20$ with likely values for γ_{min} on the order of a few. Using the results of Celotti and Fabian (1993), who showed that jets comprised mainly of an electron-proton plasma must have $\gamma_{min} \geq 100$ to avoid carrying too much kinetic energy, we suggested that 3C 279 has a primarily electron-positron plasma.

We cannot make similar arguments for the other sources until we have their circular polarization results at 22 GHz. However, we can make several observations about the presence of circular polarization in the sources we observe.

In each of the sources where we have detected circular polarization, we find it either in or very near the core. This is perhaps not too surprising given that the signals we detect are a very small fraction of the total intensity and the core is the brightest part of the jet in these sources. However, in 3C 84 we detect circular polarization not on the brightest part of the core, but rather at the base of the southern jet, which is locally a factor of 2-3 less bright than the map peak. In 3C 273 we do not detect significant circular polarization until epoch 1996.41, although the core is already very strong by epoch 1996.23. By epoch 1996.74, the circular polarization of 3C 273 is predominately associated with the emerging core component, rather than split evenly between both core components. These results can be understood from the work of Jones and O’Dell (1977), who find that circular polarization, however it is produced, is a strong function of opacity and is strongest near the $\tau = 1$ surface.

The circular polarization we observe is linked to other properties of the sources. The core of 3C 273 undergoes an outburst over the course of our observations in 1996. The May epoch observations of 3C 273 are the first in which we see significant circular polarization in this source. May is also the first epoch in which we observe linear polarization in the core of 3C 273. The simultaneous appearance of linear and circular polarization in the core of 3C 273 most likely results from the changing opacity in the core region. Figure 11 shows the spectral index of the core of

3C 273 between 15 and 22 GHz as a function of epoch (Ojha 1998). This figure demonstrates that the core begins to become significantly less opaque by the 1996.41 epoch when we first detect strong circular polarization.

The core of 3C 279 also undergoes an outburst in 1996. We observe the western core component, CW, to nearly triple in strength from January to September. The circularly polarized flux we observe in 3C 279 appears to track the rise in total flux of this component, although the uncertainty of the measurements in the 1996.23 and 1996.41 epochs makes detailed analysis of the evolution difficult.

A second result is that the *sign* of the circular polarization is constant across epoch in all of our sources. 3C 84, PKS 0528+134, and 3C 279 all have positive circular polarization while 3C 273 has negative circular polarization. 3C 84 changes very little in total intensity or linear polarization over our observations, but the other three sources undergo significant changes in flux and/or linear polarization. For the sign of the circular polarization to remain constant, there must be a stable, uni-directional component of magnetic field in the jet.

In fact, both Faraday conversion and intrinsic circular polarization require the presence of some excess uni-directional component of magnetic field. In the case of conversion, this field provides the small amount of Faraday rotation necessary for conversion. (Conversion cannot operate on pure Stokes Q.) A tangled field geometry or differential aberration (Jones, personal communication) can remove the need for Faraday rotation, but such a geometry is unlikely to produce the sign consistency we observe. It is also possible to produce some net uni-directional field stochastically, but again, it would not be expected to remain constant (in sign) while a source is undergoing large internal changes.

Single dish circular polarization observations at 8 GHz by Hodge and Aller (1977) detected about +0.1% integrated circular polarization on 3C 279, consistent in sign with our observations. They detected about –0.1% integrated circular polarization on 3C 273, also consistent with our observations. For 3C 84, they measured about –0.1% circular polarization which is opposite in sign to our observations. Future multi-frequency VLBI observations of 3C 84 will be important to determine if this sign difference is an opacity effect or reflects slow changes in the source. Their observations of 3C 279 and 3C 273 suggest that the uni-directional component of magnetic field in these sources may be stable on a time scale of decades in our frame of observation. It is possible that this is directly related to the magnetic field at the central engine (e.g. Begelman, Blandford, & Rees 1984).

It is also interesting to examine the relation of circular polarization to linear polarization. In the cores of 3C 84 and 3C 273 we observe equal or *less* linear polarization than circular polarization. The linear polarization observed, if taken as a direct measure of field order, is not enough to produce the observed circular polarization by Faraday conversion. Lack of observed linear polarization also presents a problem if the circular polarization is produced by the intrinsic mechanism which requires a significant uniform field. The most likely explanation is that external

Faraday depolarization in the nuclear region of the AGN has significantly reduced the degree of linear polarization without affecting the circular polarization. This seems to be the case for 3C 84 (Wardle 1971), and we note that Taylor (1998) reports a large rotation measure of -1900 rad/m^2 for the core of 3C 273.

7. Conclusions

We have observed parsec-scale circular polarization in the radio jets of 3C 84, PKS 0528+134, 3C 273, and 3C 279 with the VLBA at 15 GHz. For each source our detections are at the level of $\sim 0.3 - 1\%$ local fractional circular polarization. Each individual detection has a significance in the range of 3 to 10σ . The circular polarizations we observe are consistent across epoch with changes in structure clearly linked to physical changes within the sources. To confirm our detections, we have devised three calibration techniques to help mitigate our sensitivity to gain errors. We find that all three techniques give consistent and reproducible results.

Our observations of circular polarization are closely tied to the physical conditions within the radio jets. We always detect circular polarization near the region of unit optical depth. In two sources, 3C 273 and 3C 279, we observe core outbursts during 1996 and find that the circular polarization is closely tied to these events. In 3C 273 we first observe significant circular polarization in the core as the outburst is reaching its maximum, simultaneous with our first observations of linear polarization from the same region. When a new component emerges from the core of 3C 273, the circular polarization is predominately associated with it.

Circular polarization may be produced as an intrinsic component of synchrotron radiation or by the Faraday conversion of linear to circular polarization. Our observations, at a single frequency, do not distinguish between these possible mechanisms, but independent of the mechanism, the remarkable consistency across epoch of the sign of the observed circular polarization suggests the existence of a long term, stable, uni-directional component of the magnetic field. Single dish observations of 3C 273 and 3C 279 at 8 GHz by Hodge and Aller (1977) suggest that this stability in these sources may span decades in our frame of observation.

Direct imaging of circular polarization with the VLBA provides an entirely new probe of the magnetic field structure and particle spectrum of the parsec-scale radio jets of AGN. Multi-frequency observations of circular polarization will be able to distinguish between the intrinsic and Faraday conversion mechanisms for producing circular polarization. By imaging all four Stokes parameters at multiple frequencies, we can construct detailed models of the entire radiative emission and transfer through the source and begin to determine the composition and energy spectrum of the relativistic plasma within the jet.

8. Acknowledgments

We would like to thank R. Ojha for a careful reading of the manuscript. We also thank Tom Jones and Craig Walker for helpful discussions. This work has been supported by NSF Grants AST 92-24848, AST 95-29228, and AST 98-02708 and NASA Grants NGT-51658 and NGT5-50136.

A. Calibration for Circular Polarization

The VLBA is equipped with circularly polarized feeds, right (R) and left (L) at each antenna. In the absence of instrumental effects, the parallel hand correlations are linear combinations of the total intensity (I) and circular polarization (V).

$$R_i R_j = \tilde{I}_{ij} + \tilde{V}_{ij} \quad (\text{A1})$$

$$L_i L_j = \tilde{I}_{ij} - \tilde{V}_{ij} \quad (\text{A2})$$

As \tilde{V} is typically $\leq 0.01\tilde{I}$, to detect circular polarization we must measure the small difference between two large quantities and are therefore very sensitive to calibration errors. It is critical to understand and remove effects which may corrupt a circularly polarized signal or may produce spurious circular polarization. These effects include instrumental polarization, gain errors, beam squint, and baseline based effects.

A.1. Instrumental Polarization

In the leakage feed model (e.g. Roberts et al. 1994) the output antenna voltages for nominally right and left circularly polarized feeds are given by

$$V_R = G_R(E_R e^{-i\phi} + D_R E_L e^{+i\phi}) \quad (\text{A3})$$

and

$$V_L = G_L(E_L e^{+i\phi} + D_L E_R e^{-i\phi}) \quad (\text{A4})$$

where G_R and G_L are complex gains, D_R and D_L are the complex, fractional response of each feed to the orthogonal polarization, and ϕ is the parallactic angle.

The time-averaged, parallel-hand complex correlations of these voltages detected at two antennas can be expressed (Roberts et al. 1994) in terms of the stokes parameters as:

$$\begin{aligned} R_i R_j^* = & G_{iR} G_{jR}^* [(\tilde{I}_{ij} + \tilde{V}_{ij}) e^{i(-\phi_i + \phi_j)} + D_{iR} D_{jR}^* (\tilde{I}_{ij} - \tilde{V}_{ij}) e^{i(\phi_i - \phi_j)} \\ & + D_{iR} \tilde{P}_{ji}^* e^{i(\phi_i + \phi_j)} + D_{jR}^* \tilde{P}_{ij} e^{-i(\phi_i + \phi_j)}] \end{aligned} \quad (\text{A5})$$

and

$$L_i L_j^* = G_{iL} G_{jL}^* [(\tilde{I}_{ij} - \tilde{V}_{ij})e^{i(\phi_i - \phi_j)} + D_{iL} D_{jL}^* (\tilde{I}_{ij} + \tilde{V}_{ij})e^{i(-\phi_i + \phi_j)} + D_{iL} \tilde{P}_{ij} e^{-i(\phi_i + \phi_j)} + D_{jL}^* \tilde{P}_{ji}^* e^{i(\phi_i + \phi_j)}] \quad (\text{A6})$$

where \tilde{P} is the linear polarization.

To detect circular polarization it is necessary to correct the parallel-hand correlations for the D-term leakage. This is particularly important for sources with high degrees of linear polarization. Suppose the measured D-terms are related to the true D-terms in the following way.

$$D^{true} = D^{measured} + \Delta \quad (\text{A7})$$

The leakage of D-term errors into the circular polarization image can be approximated by

$$V_{leak} \sim \frac{I}{\sqrt{N_s N_a (N_a - 1)}} (2\Delta D^{meas} + \sqrt{2(N_a - 1)m_L} \Delta + \Delta^2) \quad (\text{A8})$$

where Δ and D^{meas} are rms values, m_L is the fractional linear polarization, N_a is the number of antennas, and N_s is the number of scans which are separated in parallactic angle. A factor for the number of IFs is omitted because the D-terms are strongly correlated between IFs. In the worse case scenario of no D-term correction

$$V_{leak} \sim \frac{I}{\sqrt{N_s N_a (N_a - 1)}} (\sqrt{2(N_a - 1)m_L} D + D^2). \quad (\text{A9})$$

Figure 12 is a plot of $\frac{V}{I}$ versus fractional polarization, m_L , for a point source with no intrinsic circular polarization. The D-terms have an RMS of 2.5% and were added to an originally D-term free point model created by the AIPS task UVMOD. The model was built on a 5 scan, 10 antenna observation. The D-terms were added by ‘applying’ the D-term solutions found for a recent 15 GHz VLBA observation. The ratio, $\frac{V}{I}$, was measured at the location of the I peak in the cleaned images. The slope and intercept of this plot agree well with the expected relationship.

For the observations presented in section 4, the measured D-terms are typically 1-5% with $\sim 2\%$ being most common. We estimate their errors to be about 15% of the measured D-terms, so $\Delta \sim 0.2$ to 0.8% . These errors were estimated by comparing the D-term solutions from PKS 0528+134 (which were applied to all sources) to D-term solutions found independently on other sources in the same experiment. With the D-terms corrected to this level of accuracy, $V_{leak}/I < 0.002m_L + 3 \times 10^{-5}$ in our observations.

A.2. Gain Calibration

Correct gain calibration of the R and L complex gains at each antenna is critical to the detection and measurement of circular polarization. In particular, it is the calibration of the gain

difference between the R and L feeds, best represented by the complex gain ratio, R/L, which presents the largest problem for circular polarization observations using circular antenna feeds.

Self-calibration attempts to correct the complex antenna gains by comparing the u-v data to the transform of an idealized model of the source. These solutions are found in a least-square, antenna-based manner with all of the baselines to a particular antenna used to constrain the solution. Ideally, the solutions for all antennas are found simultaneously.

For simplicity, assume that we have the correct total intensity model for a source, I_{mod} . The corresponding data may then be self-calibrated using I_{mod} in one of two ways:

- Assuming $RR = \tilde{I}_{mod}$ and $LL = \tilde{I}_{mod}$. This method derives a separate correction for the Right and Left hand systems at each antenna.
- Assuming $(\frac{RR+LL}{2}) = \tilde{I}_{mod}$ and thus deriving a single correction to be applied to both the Right and Left hand systems at each antenna.

A.2.1. Self-Calibration Assuming Zero Circular Polarization.

The first method derives a separate correction for the right and left hand systems at each antenna but assumes no circular polarization in the source. In principle this method can correct the R/L complex antenna gain ratios in the absence of real circular polarization. In the presence of real circular polarization the complex correlations are

$$R_i R_j^* = G_{iR} G_{jR}^* (\tilde{I}_{ij} + \tilde{V}_{ij}) \quad (\text{A10})$$

and

$$L_i L_j^* = G_{iL} G_{jL}^* (\tilde{I}_{ij} - \tilde{V}_{ij}). \quad (\text{A11})$$

The measured gains that the second technique finds and removes from the data will be related to the true complex gains by

$$G_{iR}^{true} = G_{iR}^{meas} g_{iR} \quad (\text{A12})$$

where the g 's are residual gains that satisfy the conditions

$$g_{iR} g_{jR}^* (\tilde{I}_{ij} + \tilde{V}_{ij}) \approx \tilde{I}_{ij} \quad (\text{A13})$$

and

$$g_{iL} g_{jL}^* (\tilde{I}_{ij} - \tilde{V}_{ij}) \approx \tilde{I}_{ij} \quad (\text{A14})$$

as well as possible across the array. Real circular polarization is additive in the RR and LL correlations, so the multiplicative gains applied by self-calibration cannot completely remove real circular polarization except when the source is a simple point in total intensity. In fact, this kind

of gain calibration may reduce and relocate real circular polarization to weaker components but *cannot create it*.

Self-calibration with the assumption of zero circular polarization can seriously modify any circularly polarized signal present in a data set. Circular polarization originating on weak components seems to be largely unmodified, while circular polarization originating on strong components is shifted (with reverse sign but the same fractional level) to the weaker components in the I image. Figure 13 shows a point double source with real circular polarization, before and after self-calibration.

For point sources, such as PKS 0528+134, real circular polarization will look simply like a difference in amplitude gain between RR and LL and will be completely removed by this procedure.

For an unequal point double, such as 3C 279, there is an inherent ambiguity about the true location of any circular polarization detected with *zero- V self-cal*. Circular polarization may have originated on either the weak or the strong component but will show up only at the location of the weak component in the *zero- V self-cal* image. Assuming the circular polarization originated on the stronger core component, it is possible to extrapolate the true circular polarization distribution. For a strongly unequal point double:

$$V_1 \simeq -V_2(I_1/I_2) \tag{A15}$$

where V_2 is the circular polarization on the weak component after self-calibration assuming zero circular polarization and V_1 is the extrapolated circular polarization of the core.

The fractional error in this extrapolated measurement of V_1 is then the same as the fractional error in V_2 which is best determined by examination of the off-peak noise in the image. In addition to this noise, our creation of model sources similar to 3C 279 showed there is a systematic loss of signal caused by the assumption of zero circular polarization on the order of 10-20%. As a result, equation A15 will extrapolate values for the core of 3C 279 that are typically 10-20% low.

For complicated sources, such as 3C 84 and 3C 273, it is much more difficult to predict the effects of assuming no circular polarization during self-calibration. In the case of 3C 84, we were fortunate because the real circular polarization appeared in the jet, off the peak in the image. As a result, *zero- V self-cal* could not seriously reduce or relocate the circular polarization without inducing larger amounts of (opposite sign) circular polarization on the map peak. We verified this by carefully creating detailed models of 3C 84. In doing so, we found that only the small negative component of circular polarization in the *zero- V self-cal* image is (in part or in whole) an artifact of assuming no circular polarization during self-calibration.

A.2.2. A Hybrid Technique: R/L Gain Transfer

The second self-calibration assumption ($(RR + LL)/2 = \tilde{I}$) makes no assumption about circular polarization in the source and accurately calibrates the average of R and L at each antenna; however, it cannot correct the R/L antenna gains crucial for detecting circular polarization. The first self-calibration assumption ($RR = \tilde{I}$, $LL = \tilde{I}$) can calibrate the R/L antenna gains but may reduce or relocate real circular polarization in the process.

A natural compromise is to solve for the R/L antenna gains only on objects which are believed not to have circular polarization, using the assumption of zero circular polarization in self-calibration, and to transfer these measurements to the other sources in the observation.

In practice, this is accomplished by first doing the complete calibration⁷ of the experiment with no assumption made about the presence or absence of circular polarization. That is, the rigorous assumption $(RR + LL)/2 = \tilde{I}$ is made for all self-calibration steps. At the end of this calibration, only the R/L antenna gain ratio remains to be calibrated for each antenna. Selected sources (which are assumed to contain no circular polarization) may then be self-calibrated with the assumption $RR = \tilde{I}$ and $LL = \tilde{I}$ to find the R/L antenna gain ratios that will be applied (in some averaged, smoothed form) to the remaining sources.

Initially, one does not know which sources have circular polarization and which do not. For experiments with a large number of sources that have well interleaved observations, it is possible to initially assume that *all* sources have no circular polarization. Self-calibration on each source will then produce a series of R/L gain corrections that are not directly applied to the sources but are merged, averaged, and smoothed on some time interval long enough to span several source changes. The resulting composite correction table can then be applied directly to the data with little fear that real circular polarization on any individual sources has strongly corrupted the results. At this point, all the sources may be imaged in circular polarization. If some sources appear to have significant circular polarization, we may go back a step and construct a new gain table which omits the influence of those sources.

The technique described here was used to produce the *gain-transfer* images presented in section 4. In the process of developing this technique we tried a range of averaging times for the R/L correction table from 4 hours to 24 hours. We found that, although the 4 hour averaging time produced images with the least noise, our main results were essentially independent of averaging time over this range. We also found (with this range of averaging times) that we obtained essentially the same results when the circularly polarized sources were allowed to contribute to the gain table, confirming that individual source effects do not strongly influence the R/L correction table if the averaging time spans several source changes.

Figure 14 shows the R/L amplitude gain ratios for IF 2 of the 1996.74 epoch. The raw and

⁷Including removal of any feed leakage terms.

averaged corrections are both presented. The R/L gain ratios have two time scales for variation. The first is a long time scale offset from unity on the order of a couple of percent. This offset varies slowly over the course of several hours up to 24 hours. The second time scale for variation is very short, on the order of a single scan. These short time scale variations typically have an rms deviation from the 24 hour mean of $\lesssim 2\%$. Our procedure for calibrating the R/L gain ratios corrects the long time scale offset but cannot correct the very short time scale fluctuations about this offset.

We can estimate the effect of these short time scale variations by assuming that the longer time scale offset has been correctly removed. The R/L antenna gain ratios can then be parameterized by a small offset, δ , from unity.

$$(R/L)_i = 1 + \delta_i \simeq \frac{1 + \delta_i/2}{1 - \delta_i/2}. \quad (\text{A16})$$

So the RR and LL correlations are

$$R_i R_j^* \simeq (1 + \delta_i/2)(1 + \delta_j/2)(\tilde{I}_{ij} + \tilde{V}_{ij}) \quad (\text{A17})$$

and

$$L_i L_j^* \simeq (1 - \delta_i/2)(1 - \delta_j/2)(\tilde{I}_{ij} - \tilde{V}_{ij}) \quad (\text{A18})$$

Then the measured V visibilities become

$$\tilde{V}_{meas} \simeq \tilde{V}_{ij} + (\delta_i/2 + \delta_j/2)\tilde{I}_{ij}, \quad (\text{A19})$$

Because the δ variations are essentially uncorrelated between antennas, scans, and IFs, we can estimate the errors in our fractional circular polarization, m_c , measurements:

$$\Delta_{m_c} \simeq \frac{\delta}{\sqrt{N_a N_s N_{IF}}} \quad (\text{A20})$$

where N_a is the number of antennas, N_s is the number of scans, and N_{IF} is the number of IFs. For our experiments $\delta \simeq 0.02$, $N_a = 10$, $N_s = 6$ to 10 , and $N_{IF} = 4$, so we expect errors $\lesssim 0.15\%$ of the local total intensity in our circular polarization measurements by gain transfer. This is consistent with the limits we see on sources which do not appear to have circular polarization.

A.2.3. Phase-Only Mapping.

Wardle and Roberts (1994) suggested mapping the closure phases of a VLBI data set to detect a circularly polarized signal. A very analogous (but simpler to implement) idea is to map only the phases of the parallel hand correlations. Phase-only mapping involves setting all of the amplitudes of the parallel hand correlations to unity and using only the phase information to construct a

circular polarization map. This method is useful because errors in the antenna amplitude gains dominate the error in the other techniques for making circular polarization images. By ignoring the amplitudes, we look for the signal directly in the phases of the data.

For simple sources, phase-only images will be anti-symmetric to first order and the true location of the circular polarization signal is ambiguous. For example, consider the case of a point double (like 3C 279) with the stronger peak, I_1 , taken to be at the map center and the weaker peak, I_2 , at position (x_2, y_2) . A small amount of circular polarization, V_0 , is located on either of the two peaks.

If V_0 coincides with the position of I_2 (the weaker component), the phase-only map is given by

$$V_P(x, y) \approx \frac{V_0}{2I_1} [\delta(x - x_2, y - y_2) - \delta(x + x_2, y + y_2)]. \quad (\text{A21})$$

If V_0 coincides with the position of I_1 (the stronger component), the phase-only map is given by

$$V_P(x, y) \approx -\frac{V_0 I_2}{2I_1^2} [\delta(x - x_2, y - y_2) - \delta(x + x_2, y + y_2)]. \quad (\text{A22})$$

These two phase-only maps differ only in the strength of the components. Without a-priori knowledge of the strength or true location of V_0 , it is not possible to distinguish between them. However, if we do know the true location of V_0 , its strength can be deduced using these expressions.

It is interesting to note that relative amplitude information is preserved in phase-only mapping, although the phase-only images are independent of the antenna amplitude gains. This seeming contradiction is due to the fact that while we have forced the RR and LL correlations to have unit amplitude (thus eliminating any dependence on antenna amplitude gains), it is the *total* amplitude of these correlations which have been set to unity. The amplitudes of individual I and V components which conspire to form RR and LL remain in the form of ratios if the source structure is more complicated than a point.

A.3. Beam Squint

Beam squint is a problem for any antenna with off-axis feed elements. The left and right hand feeds have slightly displaced primary beams. Any pointing error at the telescope will cause one feed to receive a larger signal than the other, resulting in a small, artificial amplitude difference between the RCP and LCP signals at that antenna.

For the VLBA at 22 GHz, a 7" pointing error (typical for the VLBA, Napier 1995) will result in a 1% amplitude difference between RCP and LCP signals at an antenna (Walker, personal communication). The observations presented in this paper are at 15 GHz where the problem is $(1.5)^2$ smaller due to the larger primary beams of each feed. The placement of the 15 GHz feed

in VLBA antennas is also better than the 22 GHz feed as it is not parallel to the azimuthal axis where the largest pointing errors occur (Walker, personal communication).

Fortunately beam squint will not be correlated between antennas and should vary with azimuthal antenna rotation during the observations. Any beam squint should be a pure amplitude gain error at each antenna and will be completely removed by the *zero-V self-cal* technique discussed in A.2.1. In the *gain transfer* technique, beam squint effects should show up as short term R/L amplitude variations and, as such, are already included in our error estimates for those images. Beam squint will not affect the phases of the data, and therefore images produced by *phase-only* mapping will be independent of beam squint effects.

A.4. Baseline Based Errors

Real circular polarization would be completely calibrated out of a data set by *baseline based* self-calibration which assumes $RR = \tilde{I}_{mod}$ and $LL = \tilde{I}_{mod}$. This makes it difficult to remove any residual baseline based errors from the data if we wish to detect circular polarization.

However, there is excellent evidence that the baseline based errors on the VLBA are extraordinarily small. Imaging of the nearly unresolved point source, DA 193, at 5 GHz with a dynamic range of better than 100,000 to 1 indicates that the baseline based errors are no larger than 0.1% at that frequency (Walker 1995). In our simulations we added baseline based errors much larger than this to our model data sets and found that while they increased the noise in the final circular polarization images they did not generate a spurious circularly polarized signal.

A.5. Additional Calibration Tests

The calibration checks described in this section were conducted early-on in our investigation. The results increased our confidence in our ability to calibrate for circular polarization and served as a basis for the more systematic tests and investigations described in the previous sections. We briefly present these initial tests and results here for completeness and to provide other observers with suggestions for other “common sense” checks when calibrating for circular polarization.

For epoch 1996.57, we repeated the entire calibration procedure (post fringe-fit) on the source 3C 84 for each IF channel separately, and then omitting each antenna in turn from the array. In no case did the apparent circularly polarized signal change significantly. It was present in every IF channel, and could not be attributed to the behavior of any one antenna.

We also checked the effect of incorrect subtraction of antenna feed leakage (D-terms) from the parallel hand data for the 1996.57 epoch of 3C 279. This was done by simply omitting the correction altogether and also by applying a completely incorrect set of D-terms. Both procedures increased the noise on the *zero-V self-cal* image enough that one might misinterpret the real

circular polarization of the source as noise. Correct application of the D-term solutions, however, revealed a clean (real) circular polarization signal in the *zero-V self-cal* image.

We conducted a similar test on 3C 84. In this case, the *zero-V self-cal* image created from data without the D-terms removed was nearly the same as the *zero-V self-cal* image created from data where we performed the proper D-term corrections. This is exactly what we expected for 3C 84 which has no linear polarization to leak into the circular polarization. The total intensity can still leak into the circular polarization image, but it is a much smaller effect.

Finally, we created three model sources, similar to 3C 279 in total intensity and linear polarization structure, with either no initial V , V on the core, or V on the jet component. These models contained thermal noise, D-term leakage, time-dependent complex gains, and baseline-based errors. We carried these models through our standard calibration procedures and found that we were able to detect a circularly polarized signal placed in the data. Equally important, we were unable to detect a circularly polarized signal when the model contained none.

REFERENCES

- Begelman, M. C., Blandford, R. D., & Rees, M. J. 1984 *Rev. Mod. Phys.*, 56, 255.
- Celotti, A. & Fabian, A. C. 1993 MNRAS, 264, 228.
- Cotton, W. D. 1993, AJ, 106, 1241.
- Gilbert, J. A., & Conway, R. C. 1970, Nature, 227, 585.
- Hodge, P. E. & Aller, H. D. 1977 ApJ, 211, 669.
- Jones, T. W. & O’Dell, S. L. 1977, ApJ, 214, 522.
- Jones, T. W. 1988, ApJ, 332, 678.
- Jones, T. W. personal communication.
- Leppänen, K. J., Zensus, J. A., & Diamond, P. J. 1995, AJ, 110, 2479.
- Napier, P. J. 1995. in Very Long Baseline Interferometry and the VLBA, ed. Zensus, J. A., Diamond, P. J., & Napier, P. J. ASP Conf. Ser. 82 (San Francisco:ASP),59.
- Ojha, R. 1998, Ph.D. Thesis.
- Roberts, D. H., Wardle, J. F. C., & Brown, L. F. 1994, ApJ, 427, 718.
- Taylor, G. B. 1998, ApJ, 506, 637.
- Vermeulen, R. C., Readhead, A. C. S., & Backer, D. C. 1994, ApJ, 430, L41
- Walker, R. C., Romney, J. D., & Benson, J. M. 1994, ApJ, 430, L45
- Walker, R. C. 1995. in Very Long Baseline Interferometry and the VLBA, ed. Zensus, J. A., Diamond, P. J., & Napier, P. J. ASP Conf. Ser. 82 (San Francisco:ASP),133.
- Walker, R. C. personal communication.
- Wardle, J. F. C. 1971, Astrophys. Lett., 8, 183.
- Wardle, J. F. C., & Roberts, D. H. 1994, CERS, 217
- Wardle, J. F. C., Homan, D. C., Ojha, R. & Roberts, D. H. 1998, Nature, 395, 457.
- Weiler, K. W. & de Pater 1983, ApJS, 52, 293.

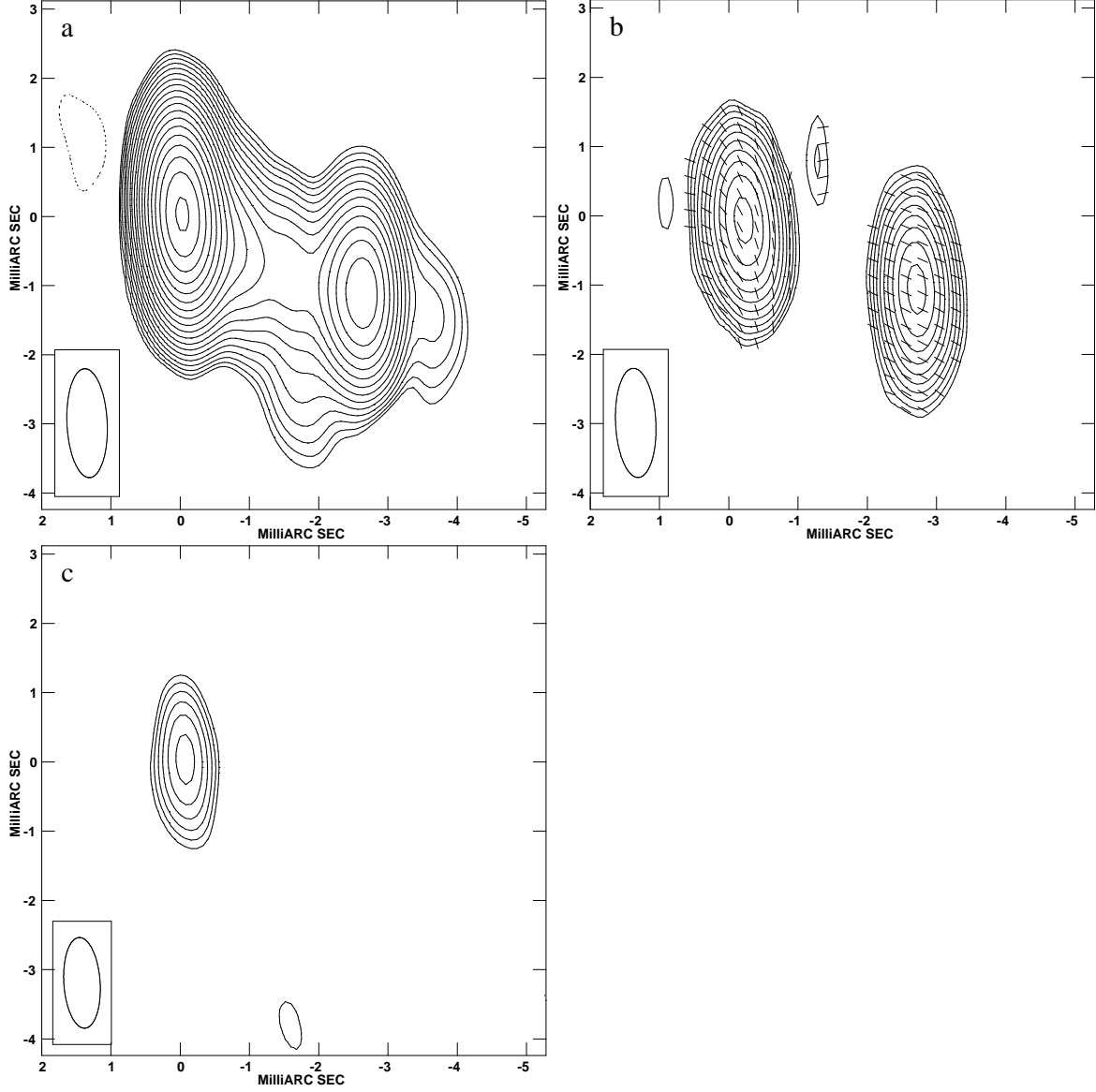


Fig. 1.— Naturally weighted images of 3C 279, January 1996. a) Total intensity $\sqrt{2}$ contours beginning at 0.02 Jy/beam. The map peak is 10.92 Jy/beam. b) Linear polarization E-vectors superimposed on polarization intensity with $\sqrt{2}$ contours beginning at 0.01 Jy/beam. The map peak is 0.36 Jy/beam. c) Circular polarization intensity $\sqrt{2}$ contours beginning at 5 mJy/beam. The map peak is 33 mJy/beam.

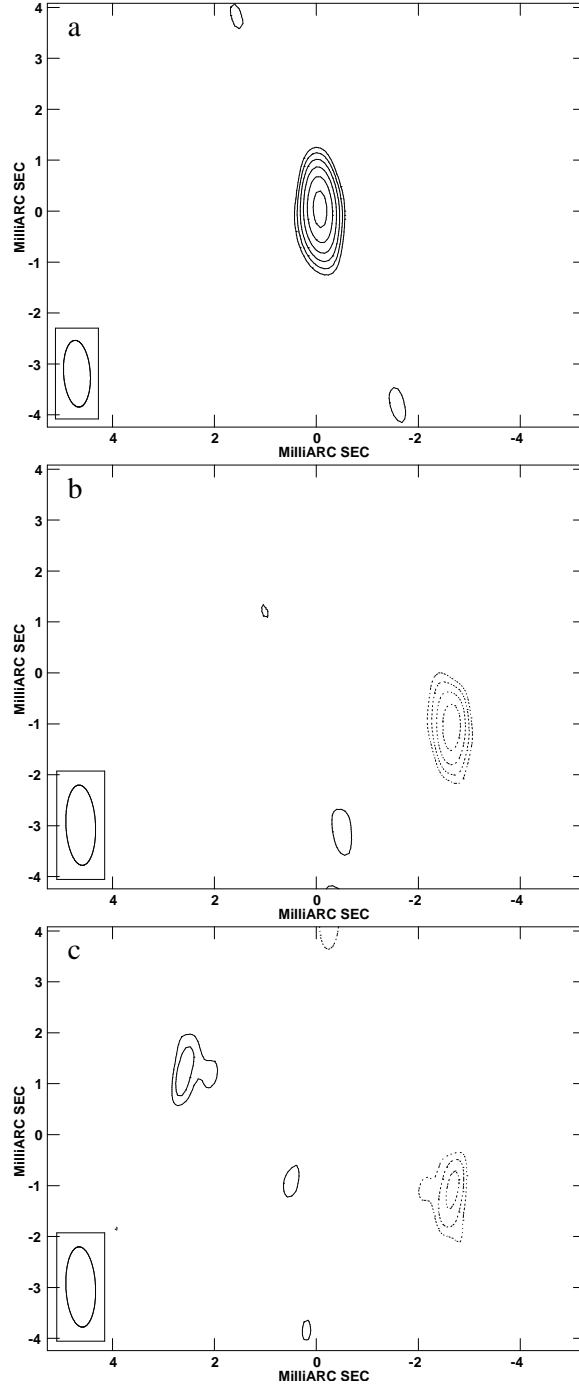


Fig. 2.— Circular polarization images of 3C 279, January 1996. a) Gain transfer calibration. $\sqrt{2}$ contours begin at 5 mJy/beam. The map peak is 33 mJy/beam. b) Zero-V self-calibration result. $\sqrt{2}$ contours begin at ± 1.4 mJy/beam. The map peak is -5 mJy/beam. c) Phase-only image. $\sqrt{2}$ contours begin at 71 μ Jy/beam. The map peak is -161 μ Jy/beam.

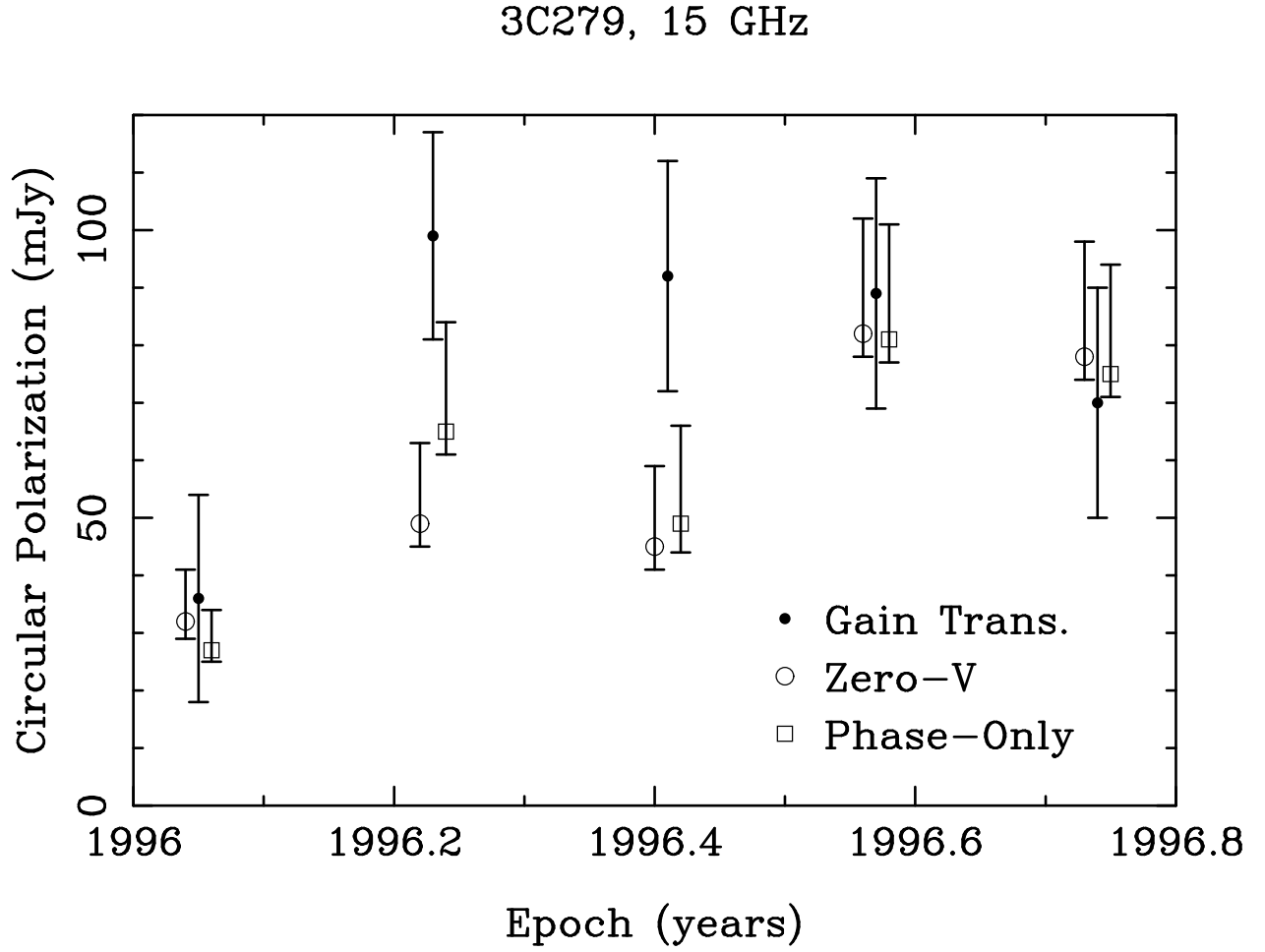


Fig. 3.— Circular polarization measurements of 3C 279. Results from all three calibration techniques are plotted versus epoch. Points for an individual epoch are slightly displaced in time to avoid confusing overlap of the error bars.

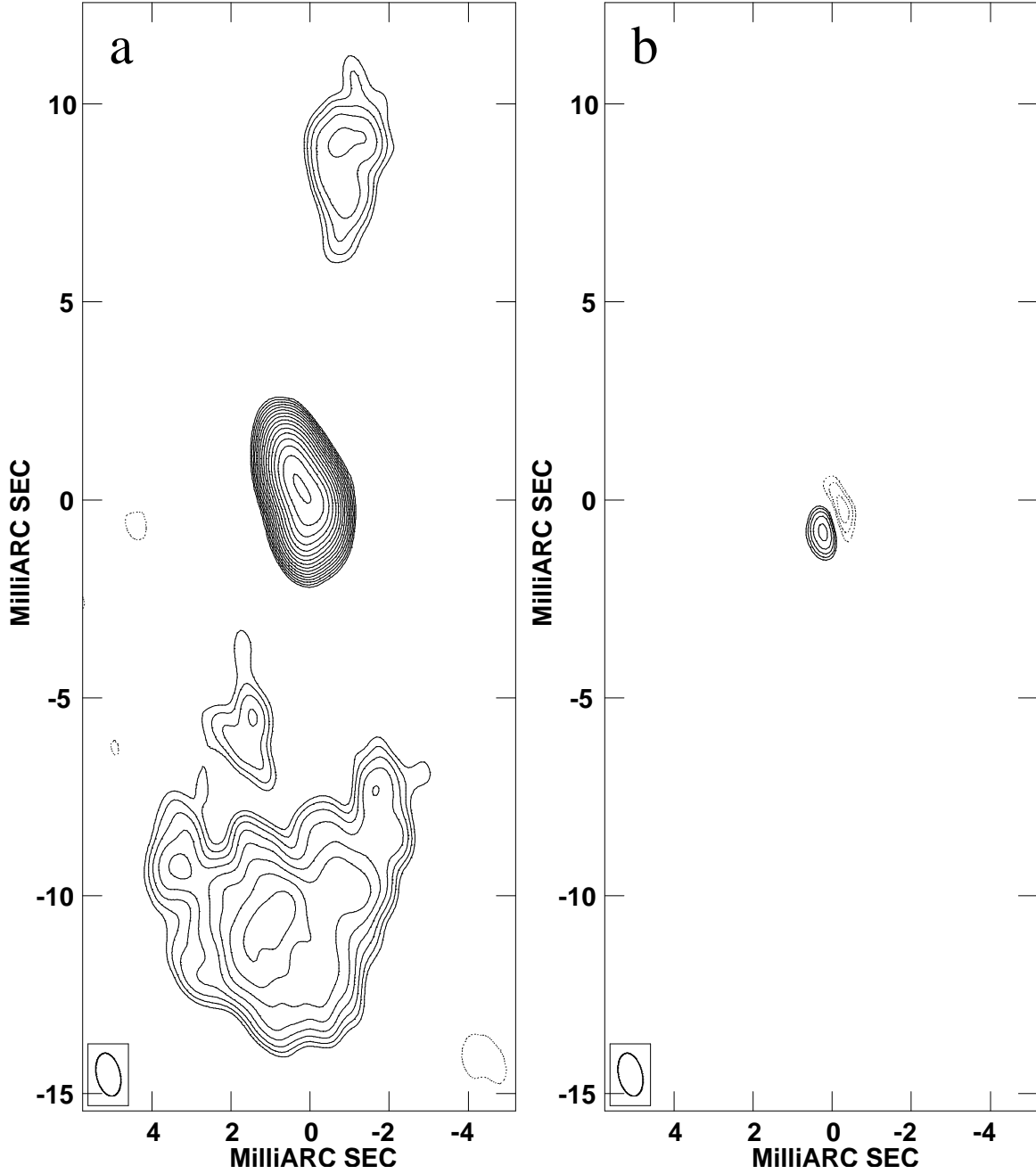


Fig. 4.— Naturally weighted images of 3C 84, September 1996. a) Total intensity $\sqrt{2}$ contours beginning at 0.020 Jy/beam. The map peak is 3.79 Jy/beam. b) Circular polarization intensity map, produced with the Zero-V self-cal technique, with $\sqrt{2}$ contours beginning at ± 4 mJy/beam. The map peak is +18.1 mJy/beam.

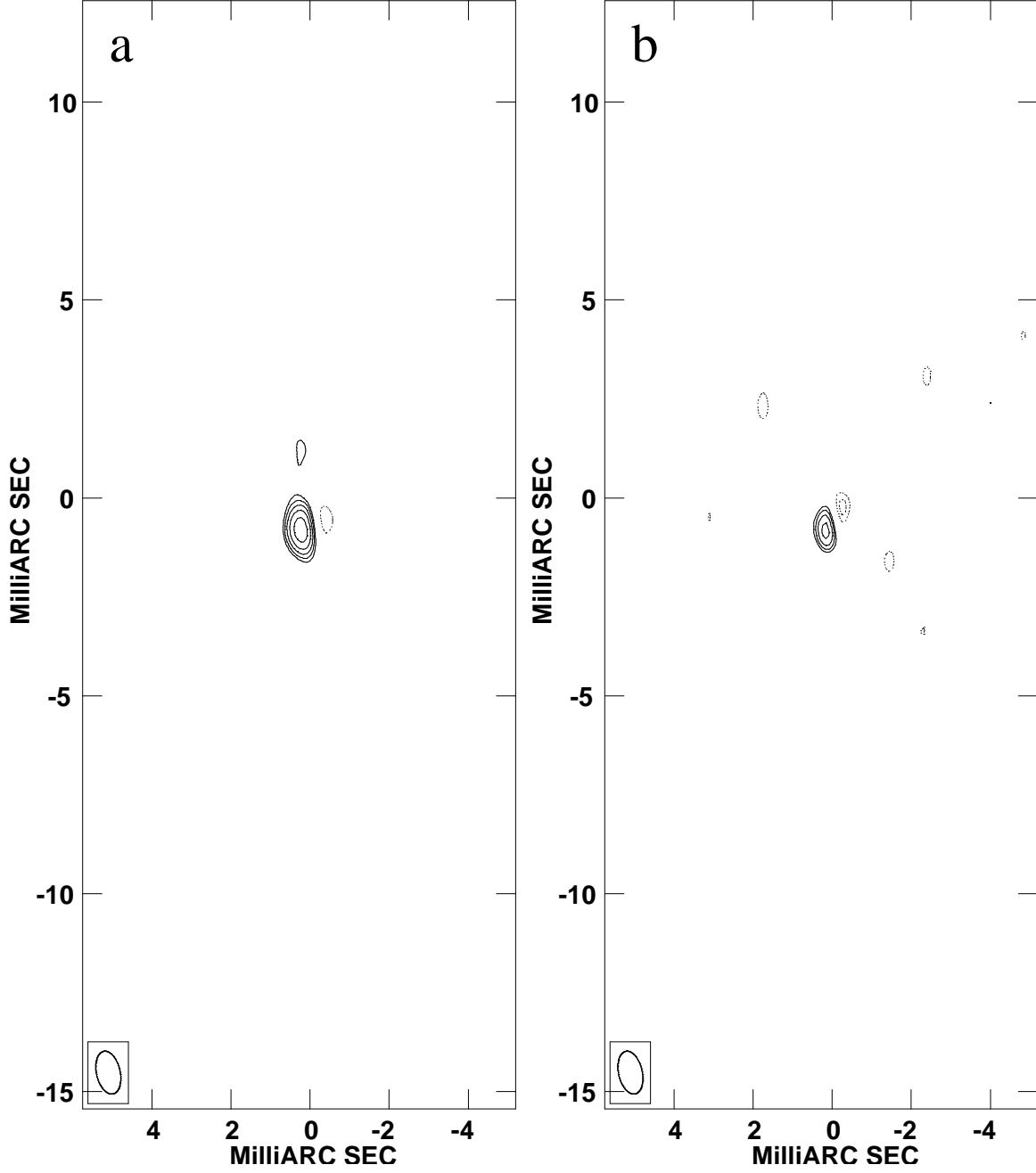


Fig. 5.— Circular polarization images of 3C 84, May 1996. a) Gain transfer calibration. $\sqrt{2}$ contours begin at ± 5.67 mJy/beam. The map peak is +28.3 mJy/beam. b) Result of phase-only mapping. $\sqrt{2}$ contours begin at ± 2 mJy/beam. The map peak is +6.4 mJy/beam.

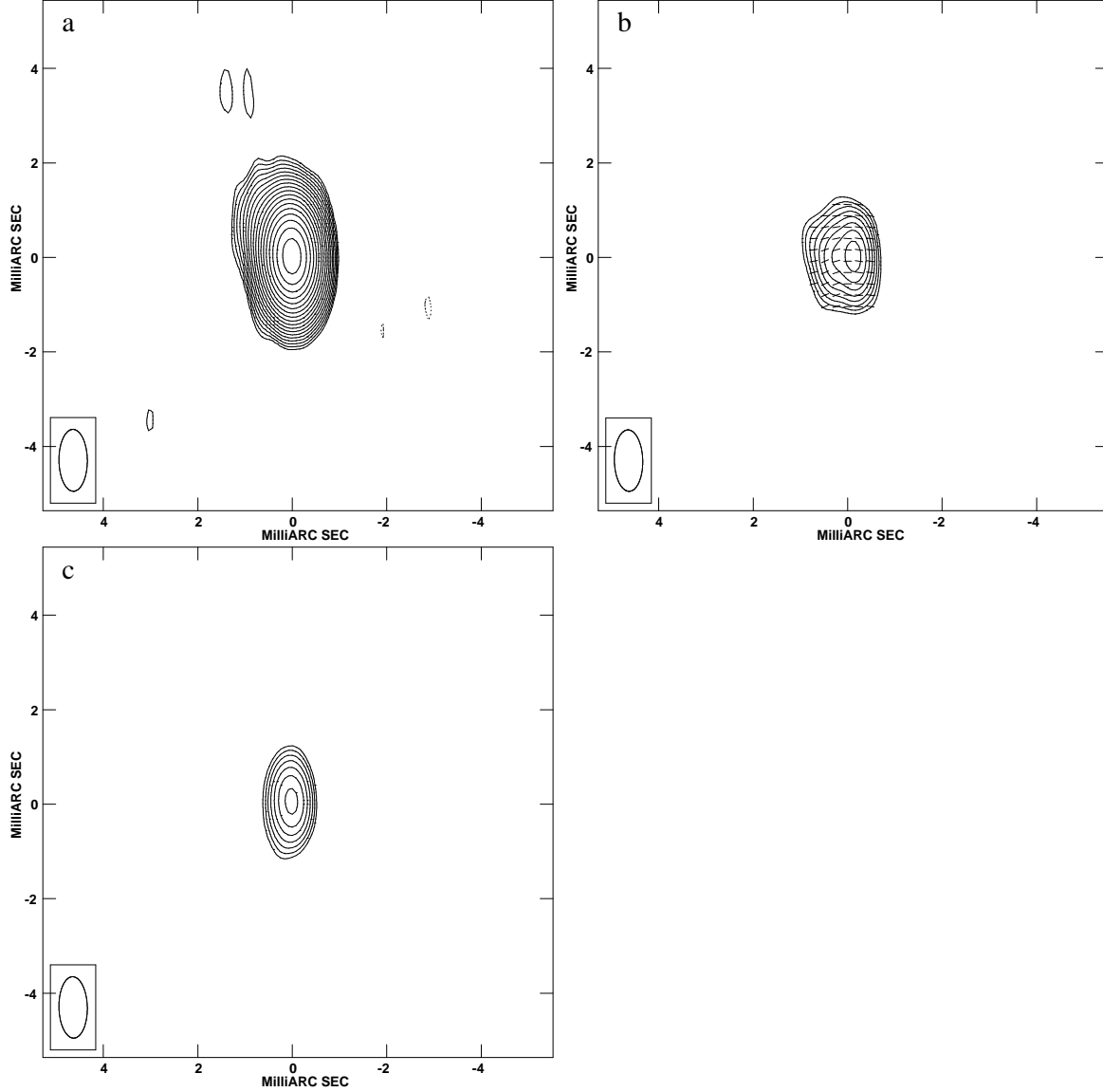


Fig. 6.— Naturally weighted images of PKS 0528+134, July 1996. a) Total intensity $\sqrt{2}$ contours beginning at 0.015 Jy/beam. The map peak is 6.78 Jy/beam. b) Linear polarization E-vectors superimposed on polarization intensity with $\sqrt{2}$ contours beginning at 0.010 Jy/beam. The map peak is 0.135 Jy/beam. c) Circular polarization intensity $\sqrt{2}$ contours beginning at 5 mJy/beam. The map peak is 45 mJy/beam.

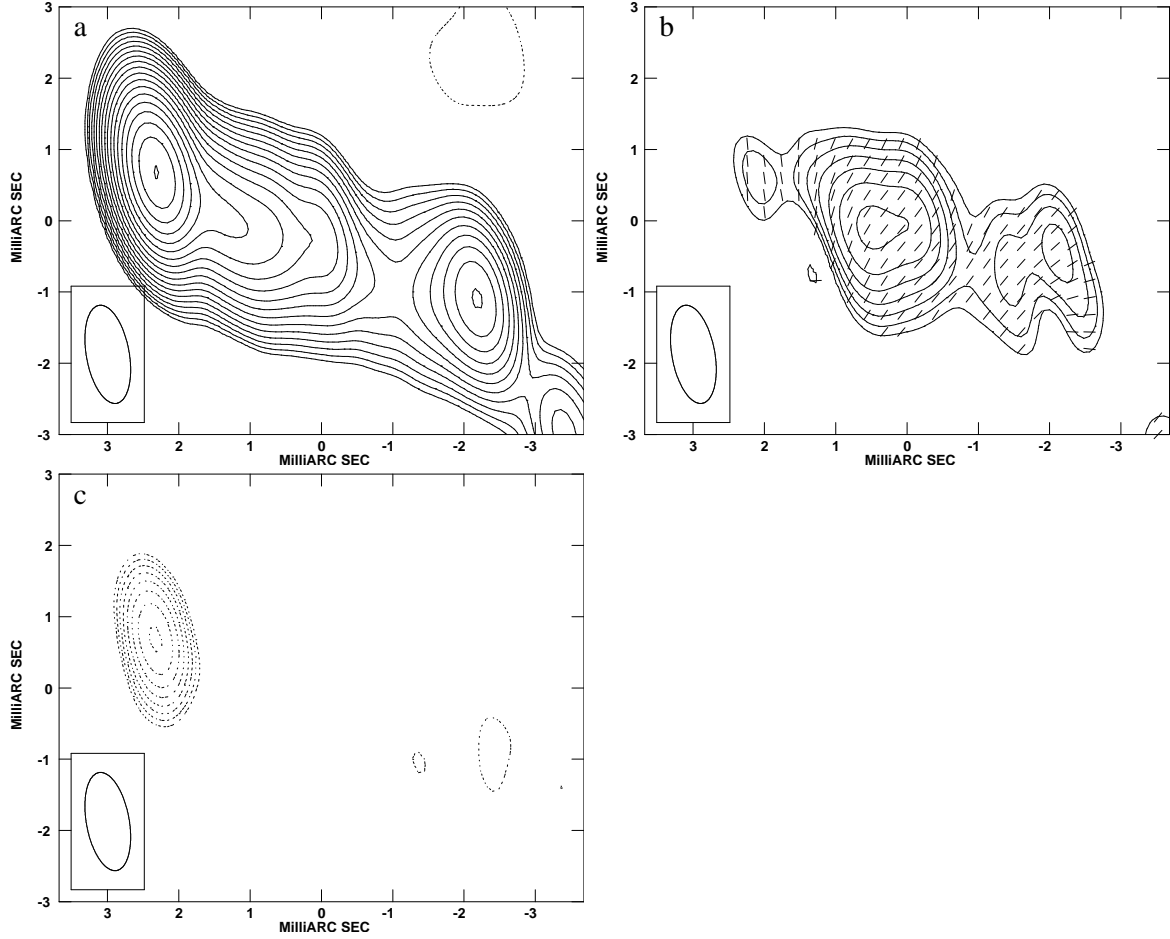


Fig. 7.— Naturally weighted images of 3C 273, May 1996. The images show only the inner 5-6 mas of the jet a) Total intensity $\sqrt{2}$ contours beginning at 0.030 Jy/beam. The map peak is 11.03 Jy/beam. b) Linear polarization E-vectors superimposed on polarization intensity with $\sqrt{2}$ contours beginning at 0.015 Jy/beam. The map peak is 0.133 Jy/beam. c) Circular polarization intensity $\sqrt{2}$ contours beginning at -5 mJy/beam. The map peak is -60 mJy/beam.

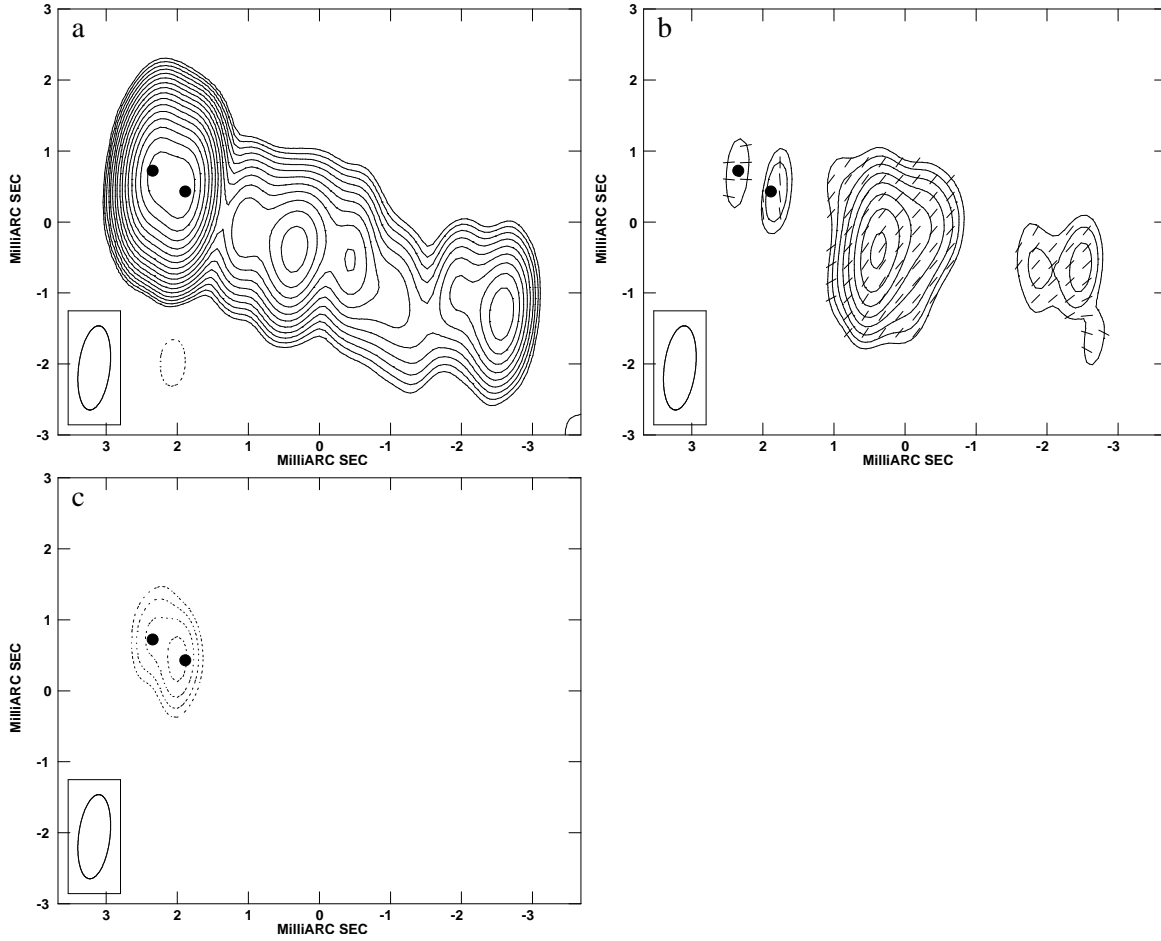


Fig. 8.— Uniformly weighted images of 3C 273, September 1996. The images show only the inner 5–6 mas of the jet. a) Total intensity $\sqrt{2}$ contours beginning at 0.030 Jy/beam. The map peak is 7.59 Jy/beam. b) Linear polarization E-vectors superimposed on polarization intensity with $\sqrt{2}$ contours beginning at 0.015 Jy/beam. The map peak is 0.184 Jy/beam. c) Circular polarization intensity $\sqrt{2}$ contours beginning at -10 mJy/beam. The map peak is -34 mJy/beam. Solid points on the images represent the locations of the eastern and western components of the core.

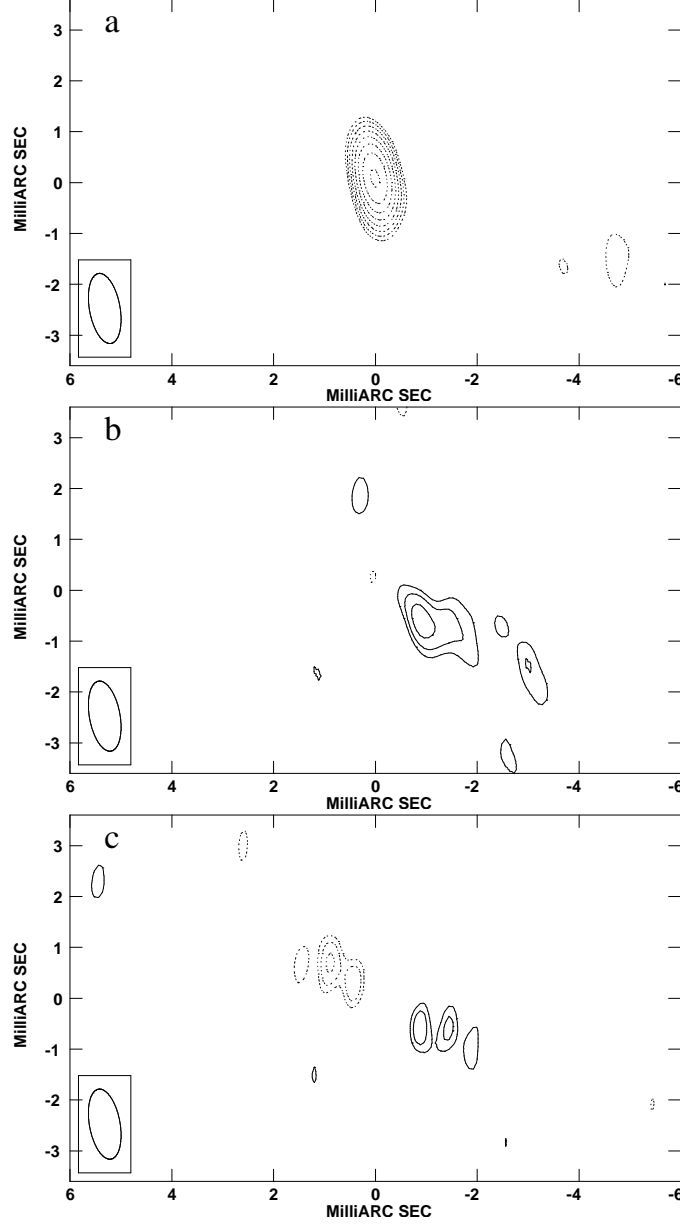


Fig. 9.— Circular polarization images of 3C 273, May 1996. a) Gain transfer calibration. $\sqrt{2}$ contours begin at -5 mJy/beam. The map peak is -60 mJy/beam. b) Zero-V self-calibration result. $\sqrt{2}$ contours begin at ± 2.0 mJy/beam. The map peak is $+5.0$ mJy/beam. c) Phase-only image. $\sqrt{2}$ contours begin at ± 140 μ Jy/beam. The map peak is $+312$ μ Jy/beam.

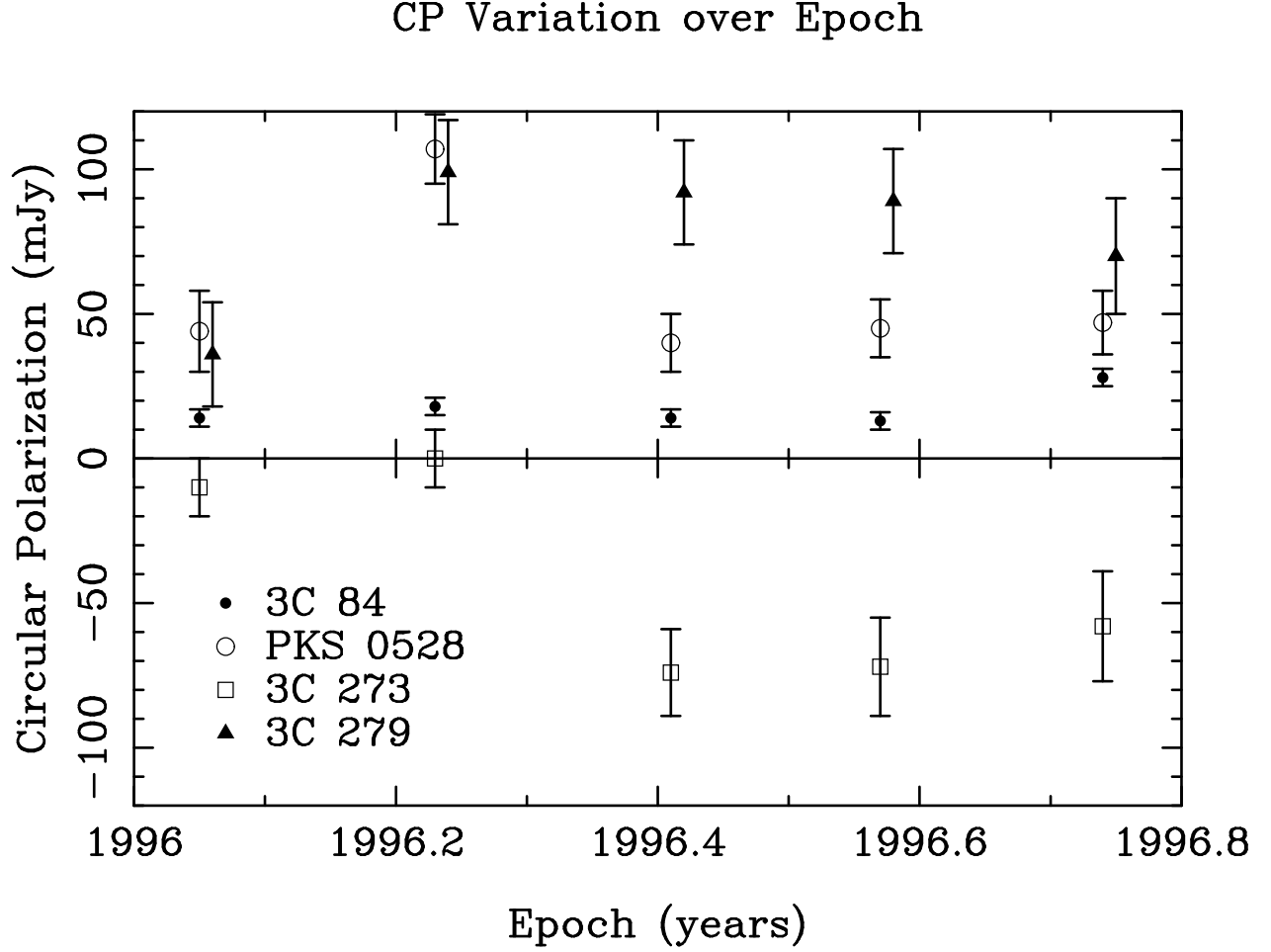


Fig. 10.— Circular polarization measurements plotted versus epoch. All measurement are from *gain transfer* calibration, excepting the 1996.57 epoch of 3C 84 for which we plot the *zero- V self-cal* measurement. The data points for 3C 279 are slightly displaced in time to avoid confusing overlap with PKS 0528+134.

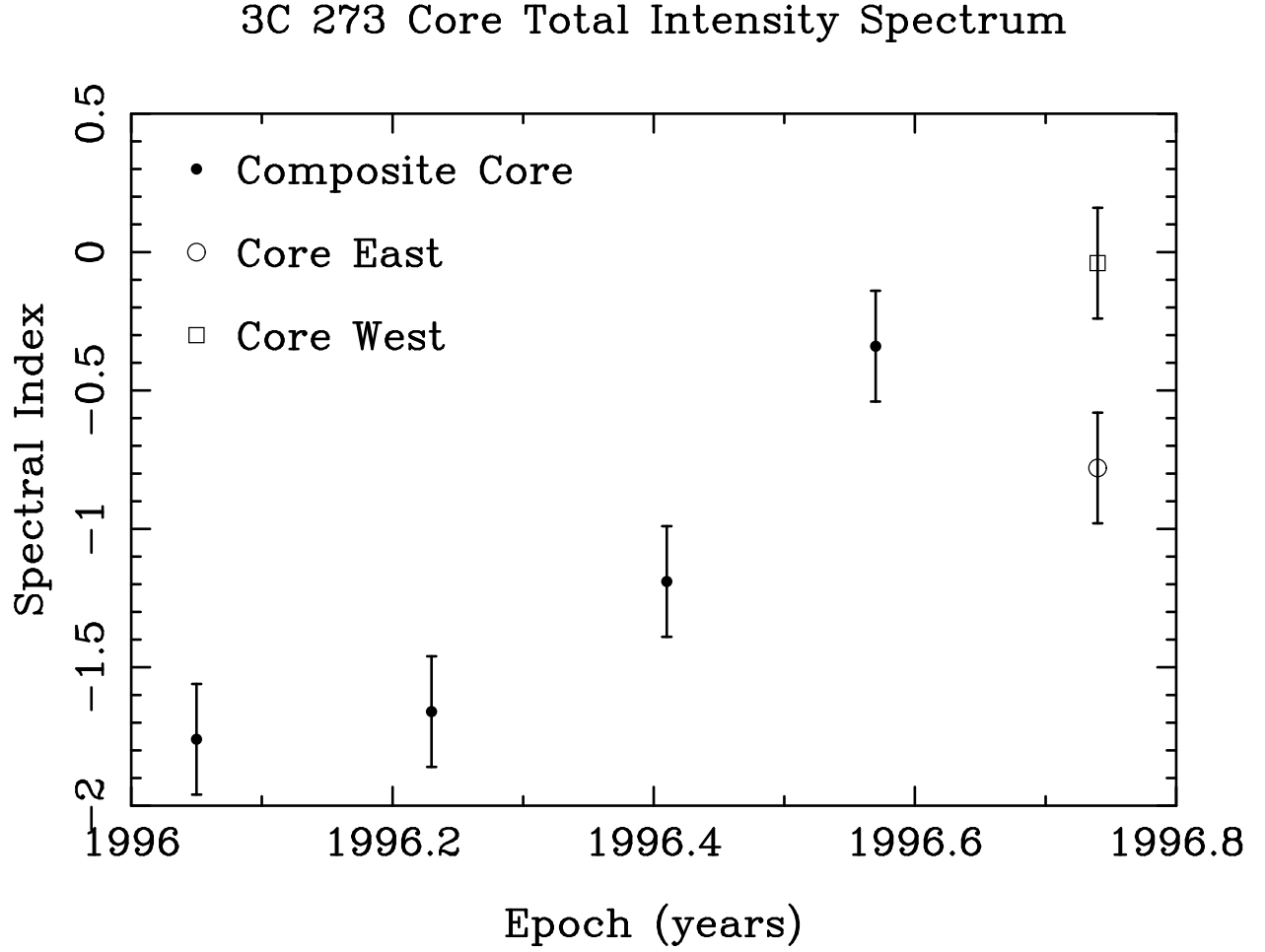


Fig. 11.— Spectral index, α , of the core of 3C 273 over time. $S \propto \nu^{-\alpha}$. α is measured between 15 and 22 GHz. In the fifth epoch, the core has separated into two pieces and the spectral index is plotted for both. “Core West” is the emerging component in that epoch.

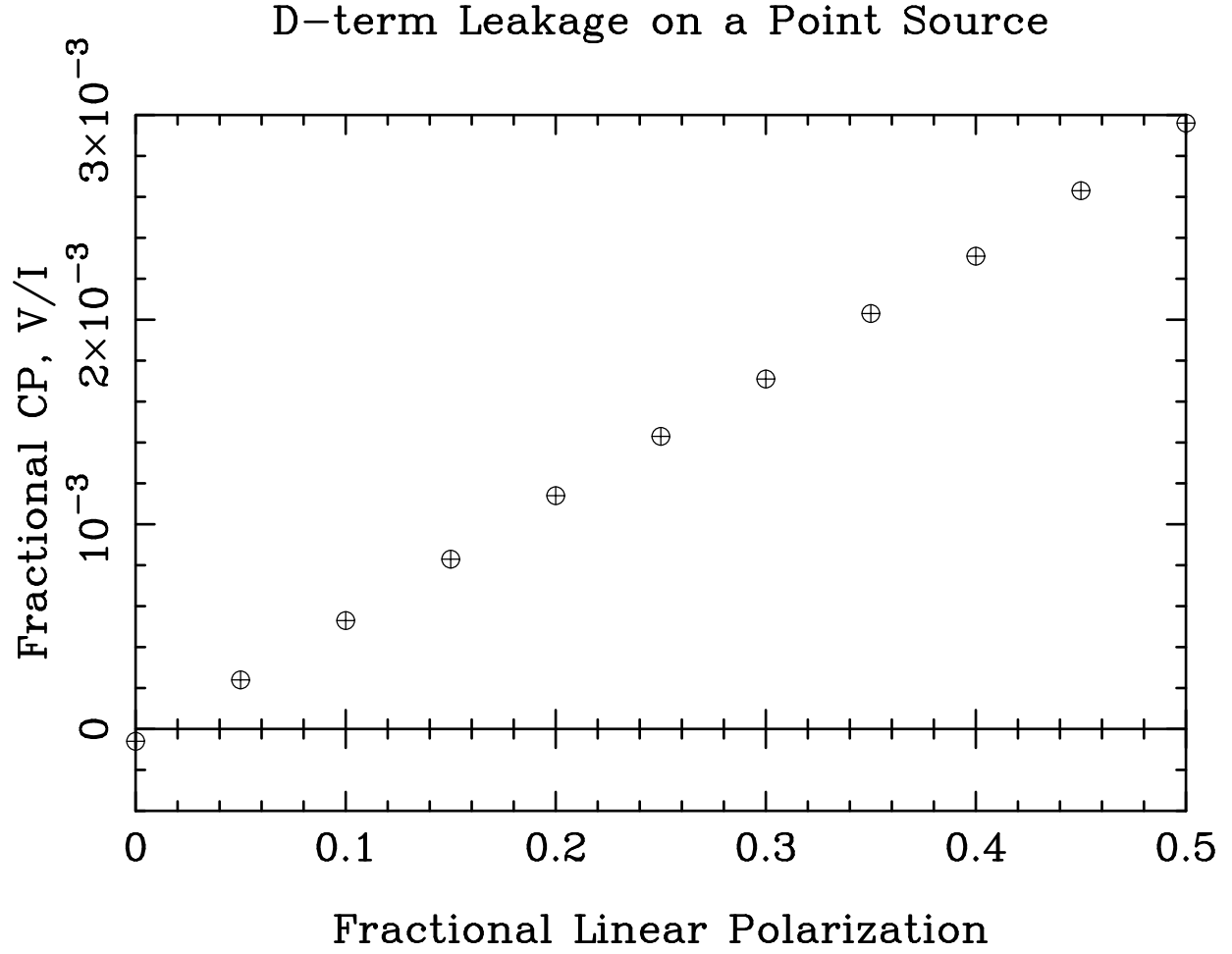


Fig. 12.— $\frac{V}{I}$ vs. fractional linear polarization for a point source with no intrinsic circular polarization. Spurious circular polarization results from leakage of uncorrected 2.5% D-terms.

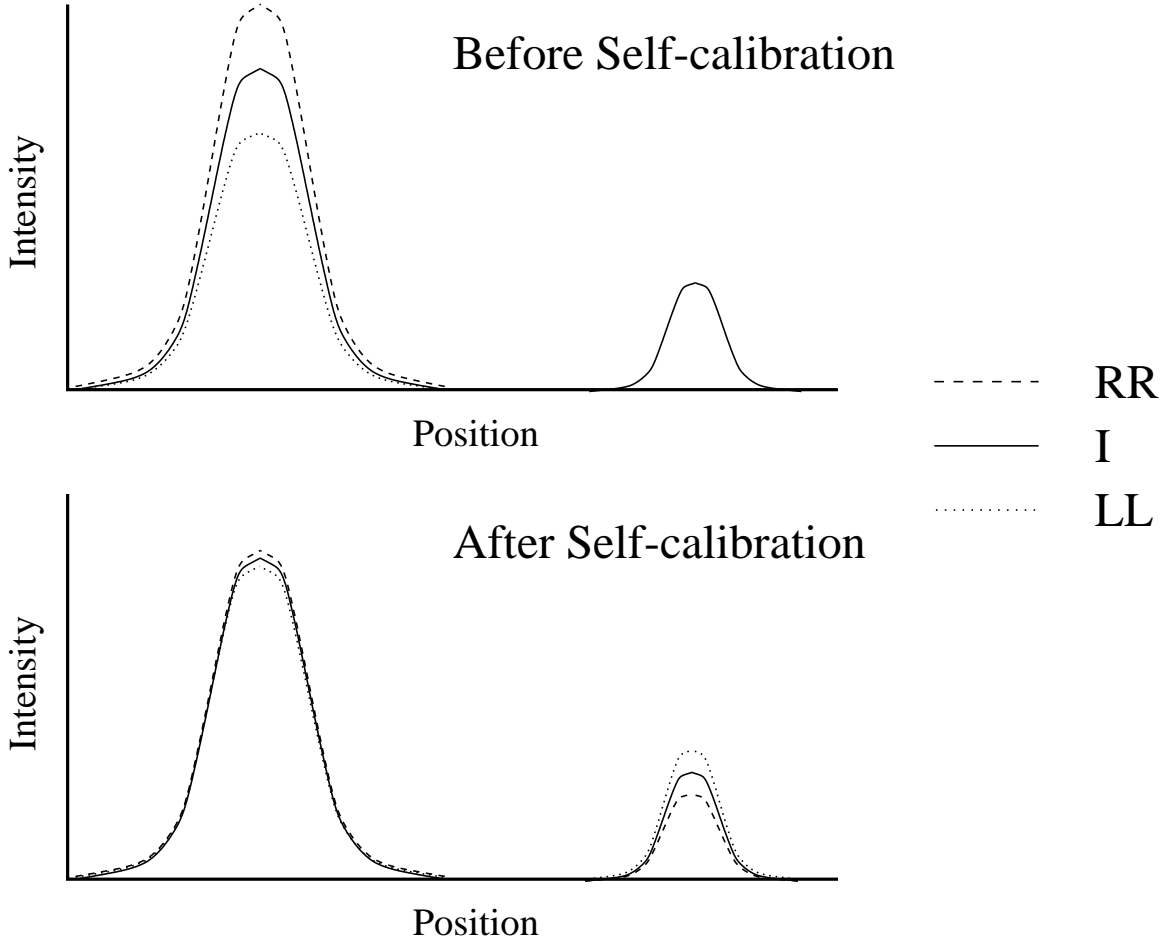


Fig. 13.— Simple graphical model of the effect of self-calibration assuming no circular polarization. The amplitudes of RR , LL , and I before and after self-calibration are illustrated. $V = (RR - LL)/2$. Before self-calibration, there is significant circular polarization on the strong I component. Self-calibration assuming no V will force RR and LL to agree with I as closely as possible by adjusting the antenna gains. Circular polarization, however, is not multiplicative but additive in the RR and LL correlations. Adjusting the antenna gains to remove the circular polarization on the strong component will induce circular polarization with the opposite sign on the weak component. So, after self-calibration, the weak component has negative circular polarization at roughly the same fractional level as the original positive circular polarization on the strong component.

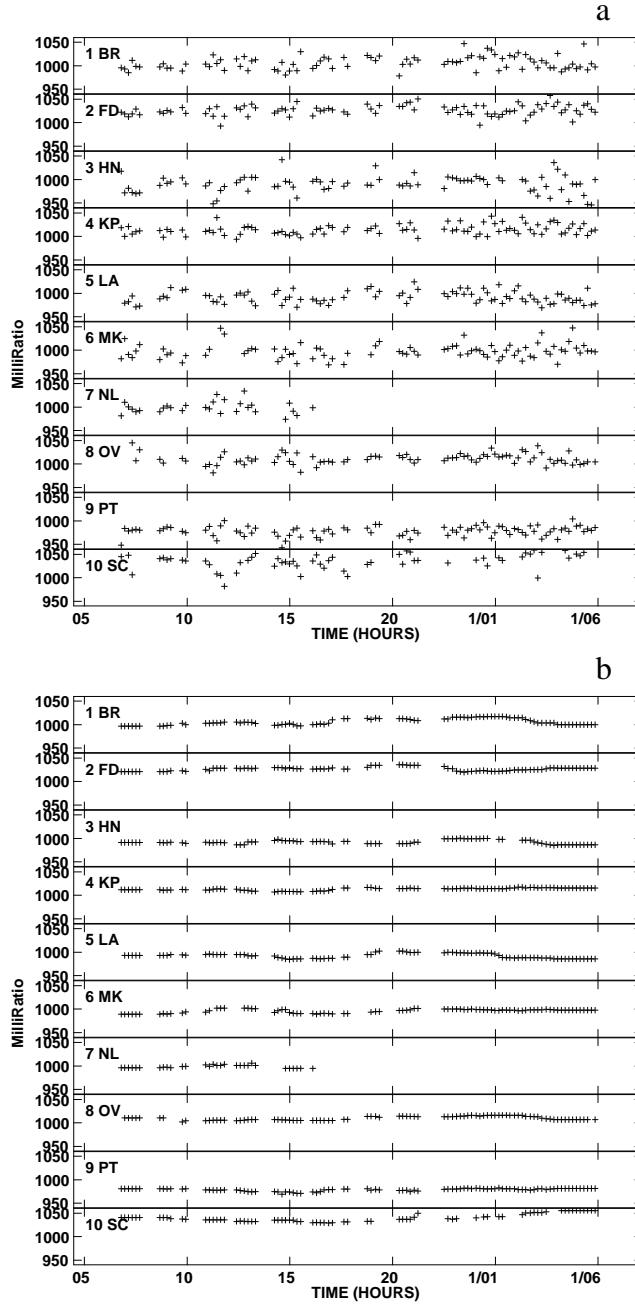


Fig. 14.— R/L amplitude gain ratio corrections for IF 2 of the 1996.74 epoch. Panel a) displays the raw corrections, before averaging and smoothing. Panel b) displays the corrections following averaging and smoothing on a 4 hour time scale.

Table 1: Epochs of observation.

<i>Date</i>	<i>Epoch</i>	<i>Notes</i>
Jan 19	1996.05	^a
Mar 22	1996.23	^b
May 27	1996.41	^c
Jul 27	1996.57	
Sep 27	1996.74	^d ^e

^aNorth Liberty antenna off-line for entire observation.

^bOwens Valley antenna off-line for first half of observation.

^cNo fringes found to the Kitt Peak antenna.

^dNorth Liberty antenna off-line for second half of observation.

^eSome data loss from the Owens Valley antenna.

Table 2: Source names and redshifts.

<i>J2000</i>	<i>B1950</i>	<i>Other</i>	<i>Redshift</i>
<i>J0319 + 41</i>	<i>0316 + 413</i>	3C 84	0.018
<i>J0433 + 05</i>	<i>0430 + 052</i>	3C 120	0.033
<i>J0530 + 13</i>	<i>0528 + 134</i>	PKS 0528+134	2.070
<i>J0738 + 17</i>	<i>0735 + 178</i>	PKS 0735+178	0.424 ^a
<i>J0854 + 20</i>	<i>0851 + 202</i>	OJ287	0.306
<i>J1224 + 21</i>	<i>1222 + 216</i>		0.435
<i>J1229 + 02</i>	<i>1226 + 023</i>	3C 273	0.158
<i>J1256 – 05</i>	<i>1253 – 055</i>	3C 279	0.536
<i>J1310 + 32</i>	<i>1308 + 326</i>		0.996
<i>J1512 – 09</i>	<i>1510 – 089</i>		0.360
<i>J1751 + 09</i>	<i>1749 + 096</i>	4C 09.56	0.322
<i>J1927 + 73</i>	<i>1928 + 738</i>	4C 73.18	0.302
<i>J2005 + 77</i>	<i>2007 + 776</i>		0.342

^aAbsorption line redshift.

Table 3: Core flux and polarization of 3C 279.

<i>Epoch</i>	<i>Component</i>	<i>R</i> (mas)	Θ (deg)	<i>I</i> (Jy)	<i>P</i> (Jy)	χ (deg)	<i>m_L</i> (%)	<i>V</i> (Jy)	<i>m_C</i> (%)
1996.05	CE	8.39	0.283	91	3.4
	CW	0.15	−117	3.12	0.672	19	21.5	+0.036 (± 0.018)	+1.2
1996.23	CE	8.53	0.379	−80	4.4
	CW	0.11	−126	5.33	0.591	24	11.1	+0.099 (± 0.018)	+1.9
1996.41	CE	9.23	1.01	−78	11.0
	CW	0.10	−115	6.80	0.944	−167	13.9	+0.092 (± 0.020)	+1.4
1996.57	CE	7.58	0.814	−83	10.7
	CW	0.09	−115	9.19	0.914	−161	9.9	+0.089 (± 0.020)	+1.0
1996.74	CE	7.08	0.825	−106	11.6
	CW	0.12	−125	9.90	0.986	6	10.0	+0.070 (± 0.020)	+0.7

Note. — Circular polarization is assumed to be associated with the CW component of the core. The circular polarization measurements are from the *gain transfer* calibration technique. The off-peak RMS noise in the circular polarization images was typically 1-2 mJy/beam; however, the errors in our measurements are limited by the short time-scale *R/L* gain fluctuations to $\lesssim 0.15\%$ of the total *I* of the core.

Table 4: Raw zero-V and phase-only results for 3C 279.

Epoch	Zero-V Self-Cal	Phase-Only Map	
	<i>V_{jet}</i> (mJy)	<i>V_{jet}</i> (mJy)	<i>V_{anti-jet}</i> (mJy)
1996.05	−5.6	−0.23	0.20
1996.23	−7.6	−0.34	0.32
1996.41	−5.4	−0.20	0.19
1996.57	−11.3	−0.37	0.34
1996.74	−11.6	−0.36	0.35

Note. — The values were obtained from model fitting with point sources in the u-v plane. The off-peak RMS noise in the *zero-V self-cal* images was typically 0.5 mJy/beam. The off-peak RMS noise in the *phase-only* images was typically 0.02 mJy/beam.

Table 5: Extrapolated CP using a simplified point double model for 3C 279.

Epoch	I Model		Zero-V Self-Cal	Phase-Only Map	Gain Transfer
	I_{core} (Jy)	I_{jet} (Jy)	Extrapolated V_{core} (mJy)	Extrapolated V_{core} (mJy)	V_{core} (mJy)
1996.05	11.40	2.02	32 (+9, −3)	27 (+7, −2)	36 ±18
1996.23	13.14	2.04	49 (+14, −4)	65 (+19, −4)	99 ±18
1996.41	15.32	1.84	45 (+14, −4)	49 (+17, −5)	92 ±20
1996.57	15.58	2.14	82 (+20, −4)	81 (+20, −4)	89 ±20
1996.74	15.57	2.32	78 (+20, −4)	75 (+19, −4)	70 ±20

Note. — Errors on these extrapolations include a positive offset for the possibility that self-calibration assuming no circular polarization may incur an overall signal loss of up to about 20% (see §A.2.1). Measurements of the circular polarization from *gain transfer* are included for comparison.

Table 6: Core flux and polarization measurements for PKS 0528+134.

<i>Epoch</i>	<i>Component</i>	<i>R</i> (mas)	Θ (deg)	<i>I</i> (Jy)	<i>P</i> (Jy)	χ (deg)	m_L (%)	<i>V</i> (Jy)	m_C (%)
1996.05	C	8.65	0.207	100	2.4	+0.044 (±0.014)	+0.5
1996.23	C	9.19	0.053	52	0.6	+0.107 (±0.012)	+1.2
1996.41	C	7.96	0.072	−42	0.9	+0.040 (±0.010)	+0.5
1996.57	C	7.76	0.137	−90	1.8	+0.045 (±0.010)	+0.6
1996.74	C	8.19	0.246	−97	2.7	+0.047 (±0.011)	+0.6

Note. — The circular polarization measurements are from the *gain transfer* calibration technique. The off-peak RMS noise in the circular polarization images was typically 1 mJy/beam; however, the errors in our measurements are limited by the short time-scale *R/L* gain fluctuations to $\lesssim 0.15\%$ of the *I* peak.

Table 7: Core flux and polarization measurements for 3C 273.

<i>Epoch</i>	<i>Component</i>	<i>R</i> (mas)	Θ (deg)	<i>I</i> (Jy)	<i>P</i> (Jy)	χ (deg)	<i>m_L</i> (%)	<i>V</i> (Jy)	<i>m_C</i> (%)
1996.05	C	2.81	< 0.010	...	< 0.3	$\sim -0.010 (\pm 0.010)$	~ -0.4
1996.23	C	6.42	< 0.010	...	< 0.2	< 0.010 (...)	< 0.2
1996.41	C	11.55	0.034	-178	0.3	-0.074 (± 0.015)	-0.6
1996.57	C	13.38	0.076	-149	0.6	-0.072 (± 0.017)	-0.5
1996.74	CE	6.51	0.035	-78	0.5	-0.019 (± 0.008)	-0.3
	CW	0.48	-120	7.81	0.039	0	0.5	-0.037 (± 0.010)	-0.5

Note. — The circular polarization measurements are from the *gain transfer* calibration technique. The off-peak RMS noise in the circular polarization images was typically 1-2 mJy/beam; however, the errors in our measurements are limited by the short time-scale *R/L* gain fluctuations to $\lesssim 0.15\%$ of the *I* peak. The *gain transfer* circular polarization result from the 1995.05 epoch is particularly noisy and has a larger estimated error.

Table 8: Core circular polarization.

<i>Source</i>	<i>Epoch</i>	<i>m_c</i> (%)	+/ <i>−</i> (%)	<i>I</i> (Jy)	<i>m_L</i> (%)	<i>χ</i> (deg)
3C 120	1996.05	< 0.3	...	1.20	0.2	−9
	1996.23	< 0.2	...	1.39	0.4	−88
	1996.41	< 0.3	...	1.22	0.3	70
	1996.57	< 0.2	...	0.85	0.0	...
	1996.74	< 0.2	...	1.47	0.1	−83
J0738+17	1996.05	~ +0.4	0.4	0.62	3.1	−61
	1996.23	< 0.4	...	0.52	1.3	−54
	1996.41	< 0.3	...	0.52	1.1	70
	1996.57	< 0.4	...	0.46	1.0	−77
	1996.74	< 0.4	...	0.49	1.7	−45
OJ287	1996.05	< 0.1	...	2.11	3.9	8
	1996.23	< 0.2	...	1.51	2.8	−8
	1996.41	< 0.2	...	1.45	2.8	−2
	1996.57	< 0.2	...	1.06	2.8	−15
	1996.74	< 0.2	...	1.49	1.9	−55
J1224+21	1996.23	< 0.2	...	1.42	5.0	−49
	1996.41	< 0.1	...	1.16	5.5	−61
	1996.57	< 0.2	...	1.16	3.9	−52
	1996.74	< 0.1	...	1.34	2.5	−49
J1310+32	1996.05	< 0.1	...	2.81	3.0	26
	1996.23	< 0.1	...	2.68	1.2	29
	1996.41	< 0.1	...	2.42	0.3	43
	1996.57	< 0.1	...	2.30	2.6	6
	1996.74	< 0.2	...	2.33	2.2	4

<i>Source</i>	<i>Epoch</i>	<i>m_c</i> (%)	+/ <i>−</i> (%)	<i>I</i> (Jy)	<i>m_L</i> (%)	<i>χ</i> (deg)
J1512-09	1996.05	< 0.2	...	0.96	1.1	7
	1996.23	~ +0.2	0.2	1.32	1.6	10
	1996.41	< 0.2	...	1.54	1.7	86
	1996.57	< 0.1	...	1.49	2.3	30
	1996.74	~ +0.2	0.2	1.18	2.2	−44
J1751+09	1996.05	~ −0.1	0.1	2.73	1.6	−71
	1996.23	< 0.2	...	1.04	3.8	−71
	1996.41	< 0.2	...	0.78	0.6	74
	1996.57	< 0.2	...	0.79	1.4	−74
	1996.74	< 0.2	...	0.86	1.1	−47
J1927+73	1996.05	~ +0.3	0.1	2.07	0.5	−82
	1996.23	~ +0.2	0.1	2.17	0.6	−32
	1996.41	< 0.1	...	2.25	1.2	−56
	1996.57	< 0.2	...	2.31	0.6	−38
	1996.74	~ +0.3	0.1	2.52	0.6	−18
J2005+77	1996.05	< 0.4	...	0.70	8.4	79
	1996.23	~ −0.4	0.4	0.63	6.3	79
	1996.41	< 0.2	...	0.55	4.1	−93
	1996.57	< 0.4	...	0.57	3.8	−84
	1996.74	< 0.3	...	0.65	4.3	−80

Note. — Measurements were made from *gain-transfer* images. The upper limits and errors are estimated to be roughly $\sqrt{2}$ times the peak noise in the images.